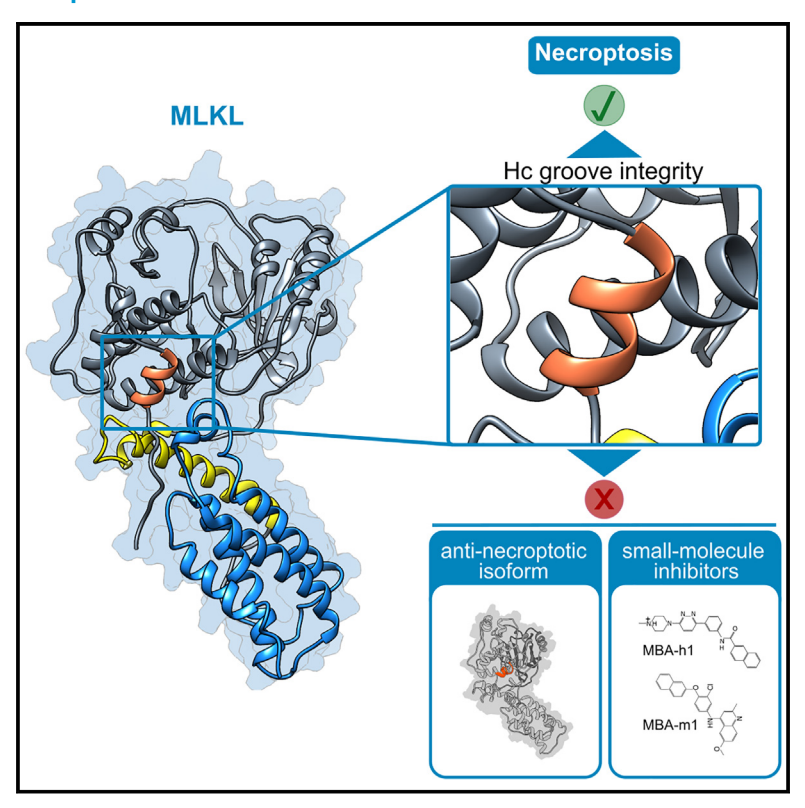
MLKL activity requires a splicing-regulated, druggable intramolecular interaction

Graphical abstract



Authors

Uris Ros, Veronica Martinez-Osorio, Pedro A. Valiente, ..., Manolis Pasparakis, Nieves Peltzer, Ana J. García-Sáez

Correspondence

uris.ros@biophys.mpg.de (U.R.), ana.garcia@biophys.mpg.de (A.J.G.-S.)

In brief

MLKL mediates plasma membrane permeabilization in necroptosis. Ros et al. show that alternative splicing inserting short sequences in the C-terminal α -helix (Hc) abolishes its killing activity, generating an anti-necroptotic isoform. Small molecules targeting the interaction of the Hc with a hydrophobic groove inhibit necroptosis in mouse models of inflammation.

Highlights

- Alternative splicing of C-terminal helix (Hc) creates an antinecroptotic MLKL isoform
- Necroptosis sensitivity is regulated in human and mice by antagonist variants of MLKL
- Hc accommodation into a hydrophobic groove is a critical switch for MLKL activation
- The Hc/groove of MLKL can be targeted with small molecules to inhibit necroptosis







Article

MLKL activity requires a splicing-regulated, druggable intramolecular interaction

Uris Ros,^{1,2,16,*} Veronica Martinez-Osorio,^{1,16} Pedro A. Valiente,^{3,14,16} Yasmin Abdelwahab,¹ Milos Gojkovic,¹ Raed Shalaby,¹ Silvia Zanna,¹ Julia Saggau,^{4,5} Laurens Wachsmuth,¹ Harshal N. Nemade,⁶ Jonathan Zoeller,² Hannah Lottermoser,⁶ Yu-Guang Chen,^{7,8} Mohamed Ibrahim,^{1,5} Konstantinos Kelepouras,^{4,5} Lazaros Vasilikos,⁹ Paula Bedoya,¹ Rafael A. Espiritu,^{10,15} Stefan Müller,¹ Veronika Altmannova,¹¹ D. Peter Tieleman,¹² John Weir,¹¹ Julian Langer,² Matti Adam,⁶ Henning Walczak,^{1,4,7} W. Wei-Lynn Wong,⁹ Gianmaria Liccardi,^{4,5} Martin Mollenhauer,⁶ Manolis Pasparakis,¹ Nieves Peltzer,^{1,5,13} and Ana J. García-Sáez^{1,2,17,*}

¹Institute of Genetics and Cologne Excellence Cluster on Cellular Stress Responses in Aging-Associated Diseases (CECAD), University of Cologne, Cologne 50931, Germany

SUMMARY

Necroptosis is an inflammatory form of regulated cell death implicated in a range of human pathologies, whose execution depends on the poorly understood pseudokinase mixed lineage kinase domain-like (MLKL). Here, we report that splicing-dependent insertion of a short amino acid sequence in the C-terminal α-helix (Hc) of MLKL abolishes cell killing activity and creates an anti-necroptotic isoform that counteracts cell death induced by the necroptosis-proficient protein in mice and humans. We show that interaction of Hc with a previously unrecognized hydrophobic groove is essential for necroptosis, which we exploited in a strategy to identify small molecules that inhibit MLKL and substantially ameliorate disease in murine models of necroptosis-driven dermatitis and abdominal aortic aneurysm. Thus, alternative splicing of microexons controls the ability of MLKL to undergo an intramolecular rearrangement essential for necroptosis with potential to guide the development of allosteric MLKL inhibitors for the treatment of human disease.

INTRODUCTION

Necroptosis is a form of regulated cell death that results in the release of danger-associated molecular patterns (DAMPs) after plasma membrane permeabilization, thereby triggering inflammation to guide immune responses. ^{1,2} Indeed, studies in genetic

mouse models provided experimental evidence that necroptosis triggers inflammation *in vivo*.^{3–5} Accumulating evidence in preclinical studies suggests that necroptosis is implicated in the pathogenesis of kidney⁶ or cardiovascular injury,⁷ cancer,⁸ neurodegeneration,⁹ autoinflammatory diseases,¹⁰ as well as in immunity to bacterial¹¹ and viral infection.^{12,13}



²Max Planck Institute of Biophysics, Frankfurt am Main 60439, Germany

³Center for Protein Studies, Faculty of Biology, Havana University, Havana 10400, Cuba

⁴Institute of Biochemistry I, Centre for Biochemistry, Faculty of Medicine, University of Cologne, Cologne 50931, Germany

⁵Center for Molecular Medicine Cologne, Cologne 50931, Germany

⁶Department for Experimental Cardiology, Faculty of Medicine, University of Cologne, and Clinic III for Internal Medicine, University Hospital Cologne, Cologne 50931, Germany

⁷Centre for Cell Death, Cancer, and Inflammation (CCCI), UCL Cancer Institute, University College London, London WC1E 6DD, UK

⁸Division of Hematology/Oncology, Department of Internal Medicine, Tri-Service General Hospital, National Defense Medical Center, Taipei 11490, Taiwan

⁹Institute of Experimental Immunology, University of Zürich, Zürich 8057, Switzerland

¹⁰Interfaculty Institute of Biochemistry, University of Tübingen, Tübingen 72076, Germany

¹¹Friedrich Miescher Laboratory and Max Planck Institute, Tübingen 72076, Germany

¹²Centre for Molecular Simulation, Department of Biological Sciences, University of Calgary, Calgary T2N 1N4, Canada

¹³Department of Genome Editing, Institute of Biomedical Genetics (IBMG), University of Stuttgart, Stuttgart 70569, Germany

¹⁴Present address: Donnelly Centre for Cellular and Biomolecular Research, University of Toronto, Toronto, ON M5S 3E1, Canada

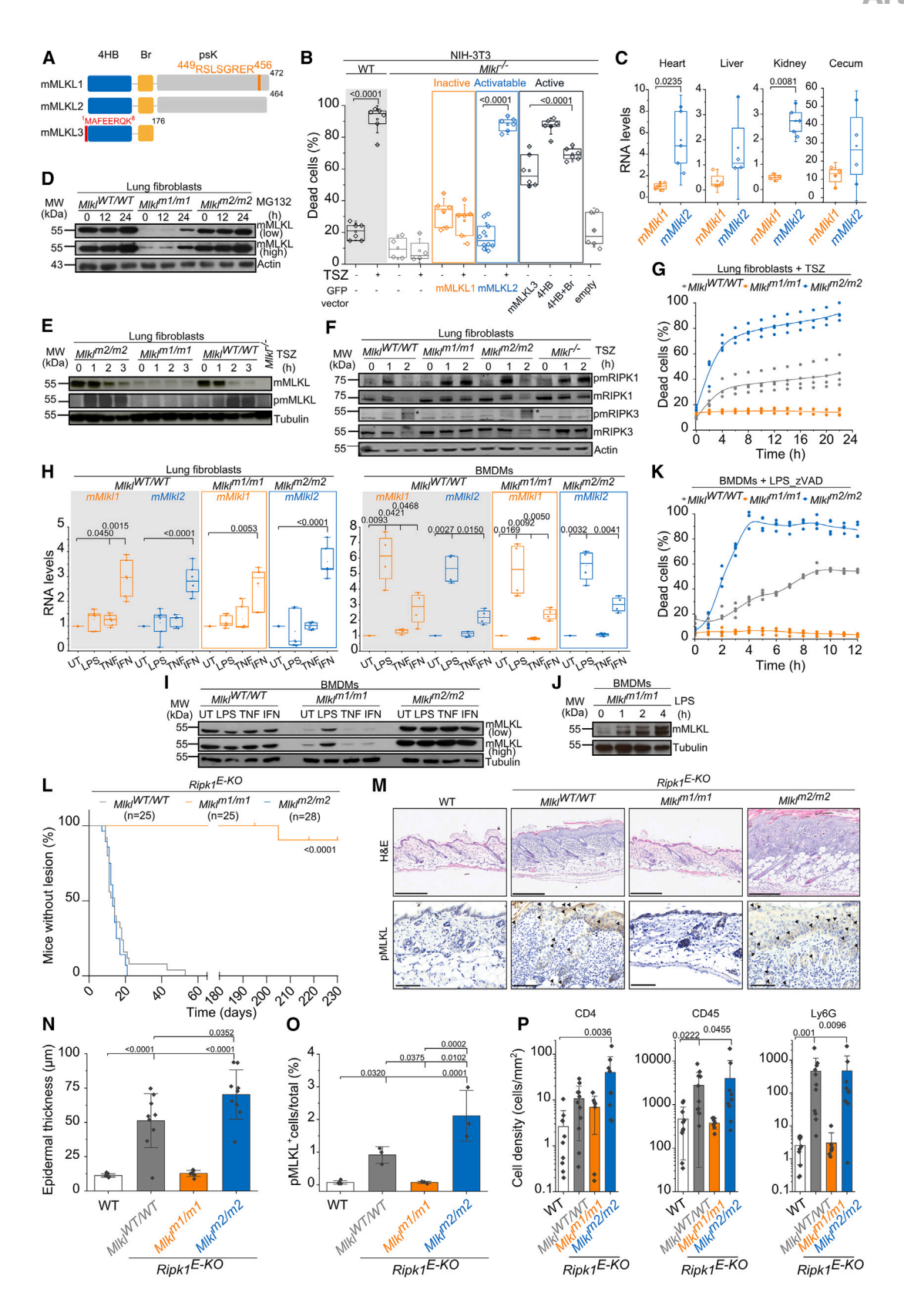
¹⁵Present address: Department of Chemistry and Translational Research and Medicine Unit, Center for Natural Sciences and Environmental Research, De La Salle University, 2401 Taft Avenue, 0922 Manila, Philippines

¹⁶These authors contributed equally

¹⁷Lead contact

^{*}Correspondence: uris.ros@biophys.mpg.de (U.R.), ana.garcia@biophys.mpg.de (A.J.G.-S.) https://doi.org/10.1016/j.molcel.2025.03.015





(legend on next page)

Article



An essential player of necroptosis is the pseudokinase mixed lineage kinase domain-like (MLKL), which is the most downstream effector of this form of cell death identified to date. 14,15 MLKL contains an N-terminal four-helix bundle domain (4HB) and a C-terminal pseudokinase domain (psK) bridged by a brace region (Br). The 4HB of MLKL acts as the killer domain, whereas the psK domain is critical to restrain the death-inducing capacity of MLKL in healthy conditions. 16 Phosphorylation by receptor-interacting protein kinase 3 (RIPK3) in the psK domain activates MLKL by inducing brace opening and 4HB exposure. 17 However, how the psK domain regulates MLKL activation remains unclear. Activated MLKL oligomerizes and translocates from the cytosol to the plasma membrane, where it induces cell death via yet unknown mechanisms. 18-20 RIPK3 itself is activated by interaction with other proteins containing a RIP homotypic interaction motif (RHIM), including receptor-interacting protein kinase 1 (RIPK1),²¹ toll/interleukin-1 receptor(TIR)-domain-containing adapter-inducing interferon-β (IFN-β) (TRIF), or Z-DNAbinding protein 1 (ZBP1). 15,22

Inhibition of the necroptotic pathway is explored for treating a range of human diseases.²³ The interest in MLKL inhibition has recently escalated because, to date, it is the only effector implicated solely in necroptosis, while targeting RIPK1 or RIPK3 also interferes with other signaling events.^{24,25} Blocking the ATP-binding site of the MLKL psK domain is used as a strategy to develop new necroptosis inhibitors, yet, this approach is limited by structural similarities with other (pseudo)kinases.^{17,26,27}

Here, we report that sensitivity to necroptosis is determined by naturally occurring splice variants of MLKL conserved in humans and mice. Alternative splicing at the C-terminal α -helix (Hc) of MLKL generates a cell death-deficient isoform that is regulated by inflammatory cues and counterbalances necroptosis induced by the necroptosis-proficient isoform. Our findings thus uncover a role for alternative splicing of microexons in regulating necroptotic cell death. Moreover, we identify the interaction of Hc with a previously unrecognized hydrophobic groove in MLKL as an essential activation mechanism. This guided the design of allosteric inhibitors for murine and human MLKL able to ameliorate

disease in mouse models of skin inflammation and abdominal aortic aneurysm, as well as to inhibit necroptosis in human cells, respectively.

RESULTS

Antagonistic MLKL isoforms determine necroptosis sensitivity

Mouse Mlkl encodes three transcript variants produced by alternative splicing (Figures 1A and S1A). mMLKL1 (UniProt: Q9D2Y4-1) only differs from mMLKL2 (UniProt: Q9D2Y4-2) in the insertion of eight additional amino acids at the C-terminal end of the psK domain of mMLKL1. mMLKL3 (UniProt: D3YV42) is a shorter isoform that lacks the psK domain but contains eight additional amino acids at the N terminus. To evaluate the necroptotic potential of the different mMLKL isoforms, we reexpressed each of them individually in Mlkl^{-/-} NIH-3T3 cells and induced necroptosis with a mixture of tumor necrosis factor (TNF), a smac mimetic compound (LCL-161) and the pan-caspase inhibitor z-VAD-FMK (zVAD) (TSZ) (Figures 1B, S1B, and S1C). Expression of mMLKL2 restored TSZ-induced necroptosis to levels seen in wild-type (WT) NIH-3T3 cells. In contrast, cells expressing mMLKL1 were completely resistant to cell death, while mMLKL3 was intrinsically active. Similar results were obtained in L929 or murine dermal fibroblasts (MDFs) when necroptosis was triggered through TNF, toll-like receptor 3 (TLR3), or TLR4 signaling pathways (Figures S1D and S1E). Mlkl^{-/-} cells reconstituted with both mMLKL1 and mMLKL2 were less sensitive to necroptosis compared with cells expressing only mMLKL2 (Figure S1F). Moreover, WT NIH-3T3 cells transfected with mMLKL2 became more sensitive to cell death compared with an empty vector, while overexpression of mMLKL1 de-sensitized necroptosis (Figure S1G).

mMLKL1 mRNA was detectable in mouse heart, liver, kidney, and cecum, yet at lower amounts when compared with mMLKL2 (Figure 1C). Next, we generated mutant mice lacking either variant by introducing specific point mutations at alternative splicing sites in exon 10 of the endogenous *Mlkl* genomic locus

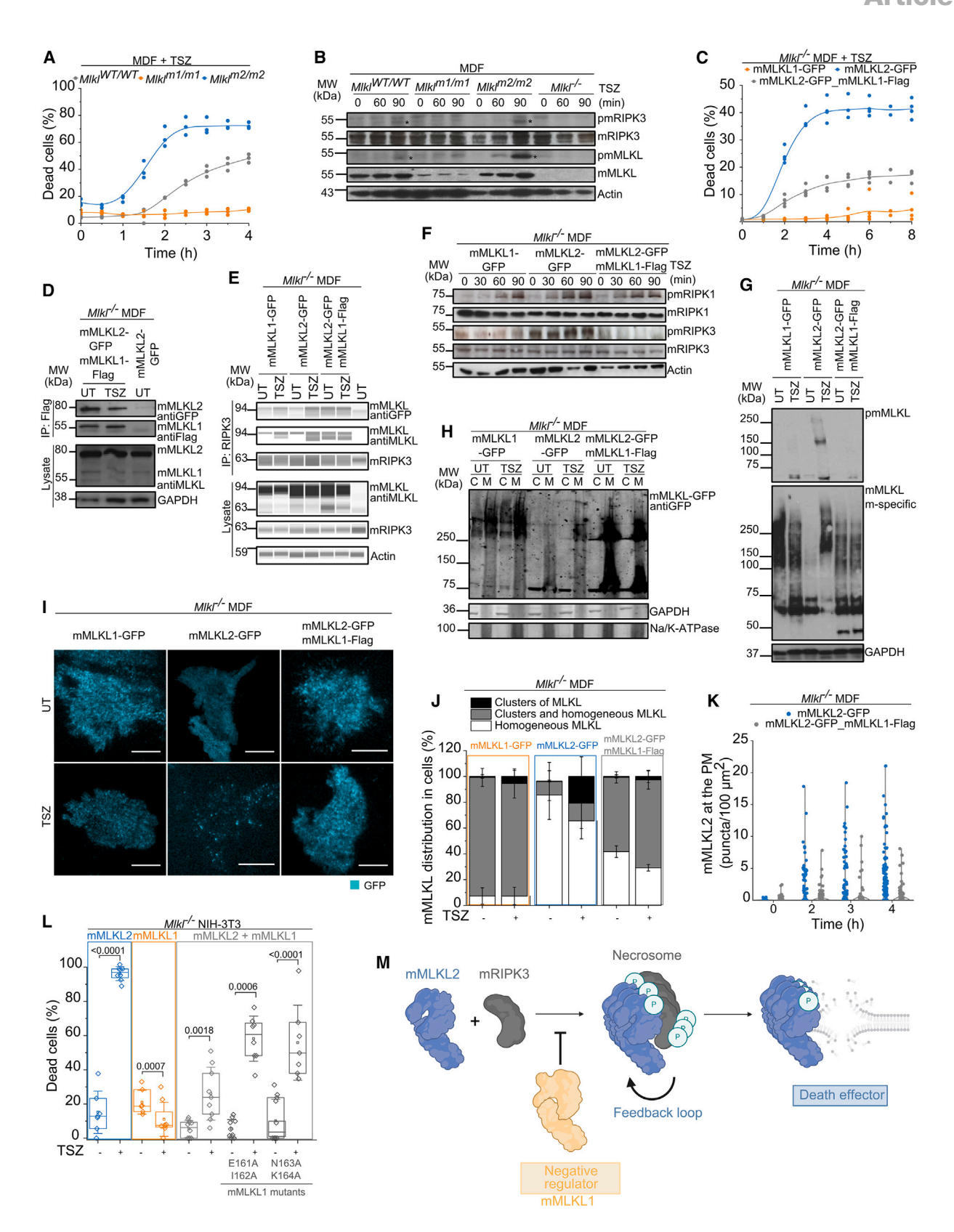
Figure 1. Mouse MLKL isoforms have different necroptotic activity

- (A) Domain representation of mouse MLKL isoforms.
- (B) Necroptosis response of MIkI^{-/-} NIH-3T3 cells transiently transfected with different variants of mMLKL-GFP.
- (C) Relative mRNA levels of mMLKL1 and mMLKL2 in different organs from mice. Data are shown as relative levels to the average of Mlkl1_mRNA detected in the heart samples.
- (D–F) Protein levels of MLKL isoforms and RIPK1/3 in primary lung fibroblasts. (D) Effect of the proteasome inhibitor MG132. (E) Total and phosphorylated MLKL. (F) Total and phosphorylated RIPK1/3.
- (G) Representative kinetics of cell death in primary lung fibroblasts upon TSZ treatment.
- (H) Change in mRNA levels of mMLKL1 and mMLKL2 in primary lung fibroblasts or BMDMs. Data are shown as relative levels to the average of Mlkl_mRNA detected in untreated samples (UT).
- (I and J) Change in protein levels of mMLKL1 and mMLKL2 in BMDMs. (I) Effect of LPS, TNF, or IFN. (J) Increase of mMLKL1 protein levels at different time points of LPS treatment.
- (K) Representative kinetics of cell death in primary BMDMs upon LPS + zVAD treatment.
- (L–P) Characterization of *Ripk1^{E-KO}* mice expressing one or the two isoforms. (L) Time of onset of skin lesions. n: number of mice. Statistics: log-rank (Mantel-Cox) and log-rank (Mantel-Cox) tests. (M) Representative images showing the haemotoxylin and eosin (H&E) staining (scale bar: 250 μm) and the pMLKL staining (scale bar: 100 μm). (N) Quantification of the epidermal thickness. Statistics: one-way ANOVA test. (O) Quantification of the pMLKL positive cells. Arrows indicate positive cells. Statistics: Holm-Šídák's multiple comparisons test. (P) Quantification of CD4, CD45, and Ly6G cells. Statistics: Kruskal-Wallis test. In (N)–(P), quantifications were calculated 3 weeks after birth.

Dots in (B), (C), (G), (H), (K), and (N)–(P) correspond to individual replicates. Whiskers ranges correspond to the SD. Bar plots are shown as main values ± SD. p values for statistically significant comparisons are shown.

Also see Figures S1 and S2.





(legend on next page)

Article



(Figures S2A and S2B), which prevented expression of mMLKL2 (Mlkl^{m1/m1}) or mMLKL1 (Mlkl^{m2/m2}). Western blot (WB) of cell lysates from lung fibroblasts isolated from WT or mutant mice allowed us to unambiguously detect endogenous protein expression of both isoforms, with consistently higher levels for mMLKL2 compared with mMLKL1 (Figures 1D, 1E, and S2C). Treatment with MG132 recovered the expression of mMLKL1 in Mlkl^{m1/m1} cells to levels comparable to mMLKL2 in Mlkl^{m2/m2} cells, indicating that mMLKL1 is efficiently translated, although its endogenous levels are kept low by turnover via proteasomal degradation.

In line with its lack of necroptosis-inducing activity, we could not detect phosphorylation of mMLKL1 upon TSZ treatment (Figures 1E and S2D). Remarkably, the levels of mMLKL phosphorylation were lower in WT compared with $Mlkl^{m2/m2}$ cells. This suggests that mMLKL1 decreases necroptosis sensitivity by reducing mMLKL2 phosphorylation and subsequent activation. Phosphorylation of RIPK3, but not of RIPK1, was abolished in $Mlkl^{m1/m1}$ and $Mlkl^{-/-}$ cells, both lacking mMLKL2 (Figures 1F and S2D). These results reveal a feedback mechanism by which mMLKL2 promotes phosphorylation of RIPK3 upstream in the signaling pathway.

Primary lung fibroblasts and bone-marrow-derived macrophages (BMDMs) containing only mMLKL1 did not respond to TSZ treatment (Figures 1G and S2E-S2H). Those carrying mMLKL2 alone were more sensitive to necroptosis than WT cells, supporting the notion that mMLKL1 antagonizes mMLKL2. We next examined the regulation of MLKL isoforms expression, in primary lung fibroblasts and in BMDMs. At the mRNA level, interferon- γ (IFN γ) induced upregulation of Mlkl1 and Mlkl2, in both cell types, while lipopolysaccharide (LPS) had the same effect only in BMDMs (Figure 1H). At the protein level, LPS induced a fast accumulation of mMLKL1, but not mMLKL2, in BMDMs (Figures 1I, 1J, S2E, and S2F), indicating the existence of regulatory mechanisms specific for mMLKL1. While Mlkl^{m1/m1} BMDMs did not undergo cell death when treated with LPS and zVAD. mMLKL1 counterbalanced the activity of mMLKL2 in WT cells (Figures 1K and S2H).

To investigate the role of MLKL isoforms in vivo, we crossed the knockin mutant mice expressing single variants with epidermis-specific RIPK1 knockout (Ripk1^{E-KO}) mice. 3,28 $Mlkl^{m1/m1}$; $Ripk1^{E-KO}$ mice, that do not express mMLKL2, did not develop any lesion (Figure 1L), similar to the reported Mlkl^{-/-};Ripk1^{E-KO}.²⁸ At the macroscopic level, we did not detect significant differences in the onset and severity of the skin lesions between Ripk1^{E-KO} and Mlkl^{m2/m2};Ripk1^{E-KO}, lacking mMLKL1 (Figure S2I). However, histological characterization of the skin samples showed increased epidermal thickness and higher levels of phosphorylated MLKL in mice expressing only mMLKL2 (Figures 1M-10). We also detected an increase in CD4-positive cells and the expression of the inflammatory cytokines interleukin (IL)-1β and IL-6 in Mlkl^{m2/m2};Ripk1^{E-KO} mice (Figures 1P and S2J). These data support the pro-inflammatory and necroptotic role of mMLKL2 in vivo. The higher levels of phosphorylated mMLKL and the thicker epidermis detected in Mlkl^{m2/m2};Ripk1^{E-KO} compared with Ripk1^{E-KO} support the inhibitory function of mMLKL1 in vivo.

Together, these findings show that, unlike mMLKL2, mMLKL1 lacks necroptosis-inducing properties. Importantly, mMLKL1 acts as an mMLKL2 antagonist so that the relative expression of the two isoforms determines necroptosis sensitivity.

mMLKL1 interacts with mMLKL2 and RIPK3 and restricts their activation during necroptosis

To gain mechanistic insight into how mMLKL1 interferes with mMLKL2, we generated immortalized MDFs expressing either mMLKL1 or mMLKL2. This system allowed studying the isoforms under endogenous, but still more consistent conditions, compared with primary cells. Accordingly, expression of mMLKL1 reduced necroptosis sensitivity (Figures 2A and S3A) and interfered with both RIPK3 and MLKL phosphorylation (Figure 2B).

To mechanistically dissect the distinct necroptotic activity of mMLKL1 and 2, we used $Mlkl^{-/-}$ MDF cells stably co-expressing both mMLKL2-GFP and mMLKL1-FLAG or only single variants tagged with GFP (Figures 2C and S3B). This allowed distinguishing MLKL isoforms in WB, as well as comparing their function and mode of action under similar protein level conditions. Both isoforms co-immunoprecipitated, demonstrating physical interaction in both basal and necroptotic conditions (Figure 2D).

Figure 2. mMLKL1 interacts with mMLKL2 and counterbalances necroptosis

- (A) Kinetics of cell death of immortalized MDF cells expressing the indicated isoforms.
- (B) Total and phosphorylated protein levels of RIPK3 and MLKL in immortalized MDF cells expressing the indicated isoforms.
- (C) Kinetics of cell death of Mlkl^{-/-} MDF cells expressing the indicated isoforms.
- (D) Fraction of mMLKL2-GFP that co-immunoprecipitated with mMLKL1-FLAG.
- (E) Fraction of mMLKL that co-immunoprecipitated with RIPK3.
- (F) Total and phosphorylated protein levels of RIPK1/3 and MLKL in Mlkl^{-/-} MDF cells expressing the indicated isoforms.
- (G) MLKL phosphorylation and oligomerization. Expression of mMLKL-GFP and cell death induction was performed as in (C). m-specific, mouse-specific antibody. Lysates were processed under non-reducing conditions.
- (H) Oligomerization and membrane translocation of mMLKL1 and mMLKL2. C, cytosolic fraction; M, microsomal fraction. Cell fractions were processed under non-reducing conditions.
- (I–K) Analysis of clusters of MLKL at the plasma membrane of living cells expressing the indicated isoforms. (I) Representative images obtained by TIRF. Scale bar: 10 µm. (J) Distribution of MLKL in the cells. (K) Density of clusters calculated at the indicated time points.
- (L) Necroptosis response of Mlkl^{-/-} NIH-3T3 cells transiently transfected with different variants of mMLKL-GFP.
- (M) Model of the divergent role of mMLKL1 and mMLKL2 in necroptosis.

Dots in (A), (C), and (L) correspond to individual replicates, and in (K), to individual cells. Whiskers ranges correspond to the SD. Bar plots are shown as main values \pm SD. p-values for statistically significant comparisons are shown. Also see Figure S3.



mMLKL2 associated with RIPK1/3 upon TSZ treatment, while mMLKL1 bound to a lower extent to RIPK3 both in healthy and necroptotic conditions (Figures 2E and S3C). Remarkably, mMLKL1 expression inhibited the increase in the interaction of mMLKL2 with both kinases during necroptosis.

RIPK3 autophosphorylation was blocked in cells lacking mMLKL2 or expressing both isoforms, confirming that this post-translational modification is dependent on mMLKL2 and reduced by mMLKL1 (Figure 2F). mMLKL2 became phosphorylated, oligomerized, and translocated to the membrane fraction in necroptosis (Figures 2G, 2H, and S3D). In contrast, mMLKL1 constitutively appeared as non-phosphorylated oligomers in both the cytosolic and membrane fractions. Only a minor fraction of monomeric and phosphorylated mMLKL1 was detected under overexpression (Figures 2G, S3E, and S3F), in agreement with its limited interaction with RIPK3. In presence of mMLKL1, a fraction of mMLKL2 also localized to membranes in healthy cells, forming non-phosphorylated, high-order oligomers (Figures 2G, 2H, and S3D). Notably, the ability of mMLKL1 to form high-order oligomers remained unchanged in cells coexpressing mMLK2.

We used single-particle, total internal reflection fluorescence (TIRF) microscopy, a type of microscopy allowing the detection of individual particles of GFP-tagged proteins at the plasma membrane of cells. In agreement with the subcellular fractionation experiments, mMLKL1-GFP formed clusters at the plasma membrane in cells treated or not with TSZ (Figures 2I and 2J). In contrast, mMLKL2-GFP appeared mostly cytosolic in untreated cells and accumulated into clusters at the plasma membrane upon necroptosis. Importantly, expression of mMLKL1 reduced the number of cells with mMLKL2-GFP clusters at the plasma membrane upon TSZ treatment, in line with the role of mMLKL1 in inhibiting mMLKL2 activation (Figure 2K).

We also investigated mMLKL isoforms ubiquitylation, a post-translational modification associated with MLKL regulation. 29,30 Using a tandem ubiquitin-binding entities (TUBEs) assay (Figure S3E), mMLKL1 appeared in a smearing pattern typical of poly-ubiquitylation, both in untreated and treated samples. In contrast, we detected a well-defined ubiquitination ladder associated with mMLKL2 activation, which was also phosphorylated, as previously reported. 29,30 In support that active MLKL is ubiquitylated, the bands corresponding to oligomeric MLKL shifted to higher molecular weights in the presence of the deubiquitinase inhibitor PR-619 (Figure S3F). Co-expression of mMLKL1 abolished the well-defined pattern of mMLKL2 ubiquitylation, in line with reduced activation (Figure S3E).

Since mMLKL1 and MLKL2 differ only in eight amino acids in Hc, we hypothesized that the protein/protein interactions identified for mMLKL1 could be mediated by the same surfaces as in mMLKL2³¹ and designed mutations in mMLKL1 that interfere with these surfaces. Concretely, we generated mMLKL1 mutants with Ala mutations in the Br, which have been reported to hamper MLKL oligomerization.³¹ While still lacking necroptotic activity (Figure S3G), these mMLKL1 mutants were unable to inhibit mMLKL2-induced necroptosis (Figure 2L). These findings support the functional relevance of protein/protein interactions for the inhibitory function of mMLKL1 and identify the Br of mMLKL1 as required for its ability to interfere with mMLKL2 activity.

Altogether, we show that the two MLKL isoforms diverge in their molecular mechanism, protein/protein interactions, and function. Unlike mMLKL2, mMLKL1 can constitutively form non-phosphorylated oligomeric species located both in the cytosol and in cellular membranes. Furthermore, mMLKL2, but not mMLKL1, is necessary to promote RIPK3 auto-phosphorylation, amplifying the enzymatic activity of the necrosome via a positive feedback mechanism when necroptosis is induced. mMLKL1 is however able to reduce the interaction of mMLKL2 with RIPK3 and, thereby, the necrosome activity. Our findings thus indicate that mMLKL1 represents a natural suppressor of necroptosis that restricts the ability of mMLKL2 to mediate necroptosis (Figure 2M).

Accommodation of Hc into a hydrophobic groove in mMLKL2 is required for its necroptotic activity

To get insight into the structural basis for the functional differences between mMLKL1 and mMLKL2, we used molecular dynamics (MD) simulations to refine the 3D models of each isoform, built based on the crystal structure of mMLKL2 (PDB: 4btf). 16 Comparative analysis predicted that the Hc of inactive mMLKL1, but not that of mMLKL2, would be partially unfolded due to the extra amino acids (Figures 3A and 3B), in line with alternative splicing often involving disordered regions. 32 Accordingly, insertion of 2, 4, 6, or 8 Ala residues at the equivalent position in Hc inactivated exogenously expressed mMLKL2, indicating that the effect is not sequence specific (Figures 3C and 3D). Deletion of the Hc and the consecutive C terminus residues (Δ448-464) also rendered mMLKL2 completely inactive (Figures 3C and 3E). These mutants were expressed at similar levels of mMLKL2 (Figure S4A), discarding this as a cause for the lack of activity. These findings demonstrate a key role for the Hc that, in contrast to previous assumptions,33 is necessary to relieve repression of the active 4HB region.

Inspection of the mMLKL2 structure predicted that the Hc is accommodated into a previously unrecognized hydrophobic groove connecting it with residues from the 4HB, the Br, and the psK domain (Figures 3A, 3B, and S4B). These interactions were disrupted in mMLKL1, supporting a central role of the Hc/ groove in MLKL activation. To examine experimentally whether Hc/groove association affected mMLKL activity, we designed the mutant mMLKL2_L450R_S454R that would disrupt the Hc based on MD simulations (Figures 3B and S4B). Accordingly, this mutant was inactive when re-expressed in mMLKLdeficient cells treated with TSZ, at comparable expression levels (Figures 3E, S4C, and S4D). mMLKL2_L450R_S454R was still phosphorylated by RIPK3, suggesting that the Hc/groove interaction is crucial for mMLKL2 activation, regardless of its phosphorylation state (Figure S4E). To further validate our prediction that interaction of Hc with the hydrophobic groove stabilizes the active conformation, we introduced double Cys substitutions designed to stabilize the Hc inside the groove through S-S bonds. Accordingly, these mMLKL2 mutants became intrinsically active, bypassing the upstream machinery of necroptosis (Figure 3F).

To define a potential role for differences in phosphorylation on the divergent necroptotic activity with mMLKL2, we modeled phosphomimetic versions of mMLKL2 (pmMLKL2) and mMLKL1 (pmMLKL1) by mutating specific positions within the psK



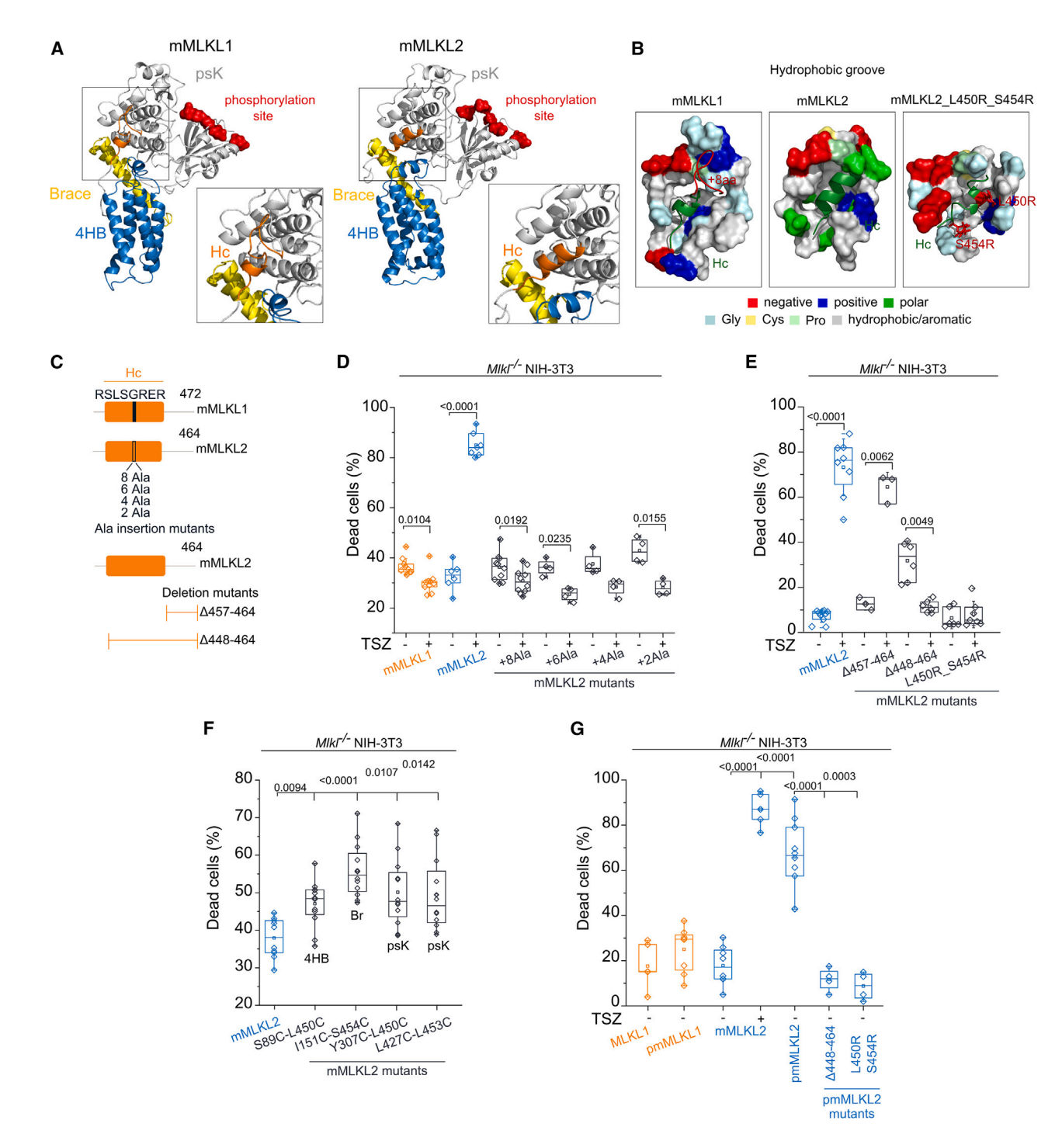


Figure 3. Accommodation of the Hc into a hydrophobic groove of mMLKL is required for necroptosis

(A) Models of the 3D structure of mMLKL1 and mMLKL2.

Dots correspond to individual replicates and whiskers ranges to the SD. *p* values for statistically significant comparisons are shown. Also see Figure S4.

⁽B) Hydrophobic groove of mMLKL1 and mMLKL2 and the mutant mMLKL2_L450R_S454R.

⁽C) Ala insertion and C-terminal deletion mutants.

⁽D–F) Necroptotic activity of $Mlkl^{-/-}$ NIH-3T3 cells transfected with GFP-tagged mMLKL mutants. (D) mMLKL2_Ala mutants. (E) mMLKL2_C-terminal deletion mutants and mMLKL2_L450R_S454R. (F) Double Cys mutants of mMLKL2 at the indicated positions connecting the Hc with the 4HB, the brace, or the psK domain. (G) Necroptotic activity of $Mlkl^{-/-}$ NIH-3T3 cells transfected with GFP-tagged mMLKL1 and 2 phosphomimetic mutants (S345D_S347D) bearing additional mutations in the Hc/groove.



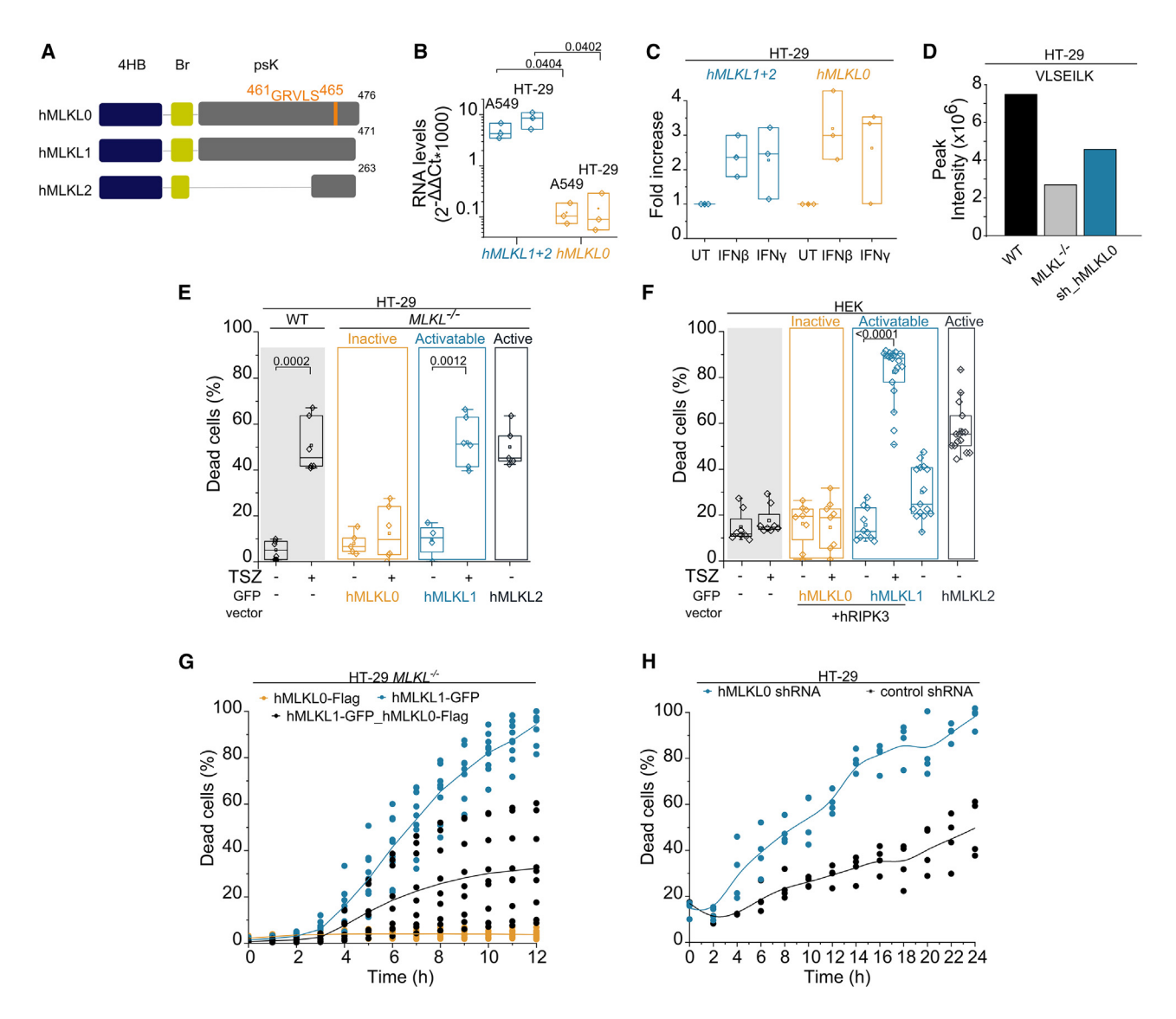


Figure 4. Inactive MLKL isoform is conserved in humans

(A) Domain representation of human MLKL isoforms.

(B and C) mRNA levels of hMLKL1+2 and hMLKL0, assessed by qPCR. (B) Levels in WT A549 and WT HT-29 cells. (C) Change in mRNA levels in WT HT-29 cells upon treatment with IFN. Data in (C) are shown as relative levels to the average of MLKL_mRNA detected in UT samples.

(D) Detection of the specific VLSEILK peptide of the hMLKL0 isoform in WT, MLKL^{-/-} and hMLKL0 knockdown HT-29 cells. sh_hMLKL0: small hairpin RNA for hMLKL0.

(E and F) Necroptotic activity of different isoforms of hMLKL in *MLKL*^{-/-} HT-29 (E) and HEK (F) cells transfected with GFP-tagged MLKL versions. (G) Effect of hMLKL0-FLAG on the necroptosis activity of hMLKL1-GFP.

(H) Effect of knockdown of hMLKL0 on necroptosis sensitivity of WT HT-29 cells. shRNA: small hairpin RNA.

Dots in (B), (C), and (E)–(H) correspond to individual replicates and whisker ranges to the SD. p values for statistically significant comparisons are shown. See also Figure S5.

domain^{34,35} (Figure 3A). We predicted that pmMLKL2 undergoes large structural reorganization involving the Hc/groove and the Br (Figures S4B and S4F–S4I). Instead, both mMLKL1 and pmMLKL1 were predicted to have similar conformational dynamics within the Hc/groove. Accordingly, phosphomimetic mMLKL2_S345D_S347D was constitutively active, while mMLKL1, as well as the mutants mMLKL2_Δ448–464 and

mMLKL2_L450R_S454R, remained inactive when similar phosphomutations were introduced (Figures 3G and S4A).

These findings indicate that the Hc/groove interaction is essential for the necroptosis-inducing capacity of mMLKL and provide a mechanistic explanation for the functional differences between mMLKL1 and mMLKL2. Altering the Hc/groove integrity interferes with the molecular switch driven by phosphorylation

Article



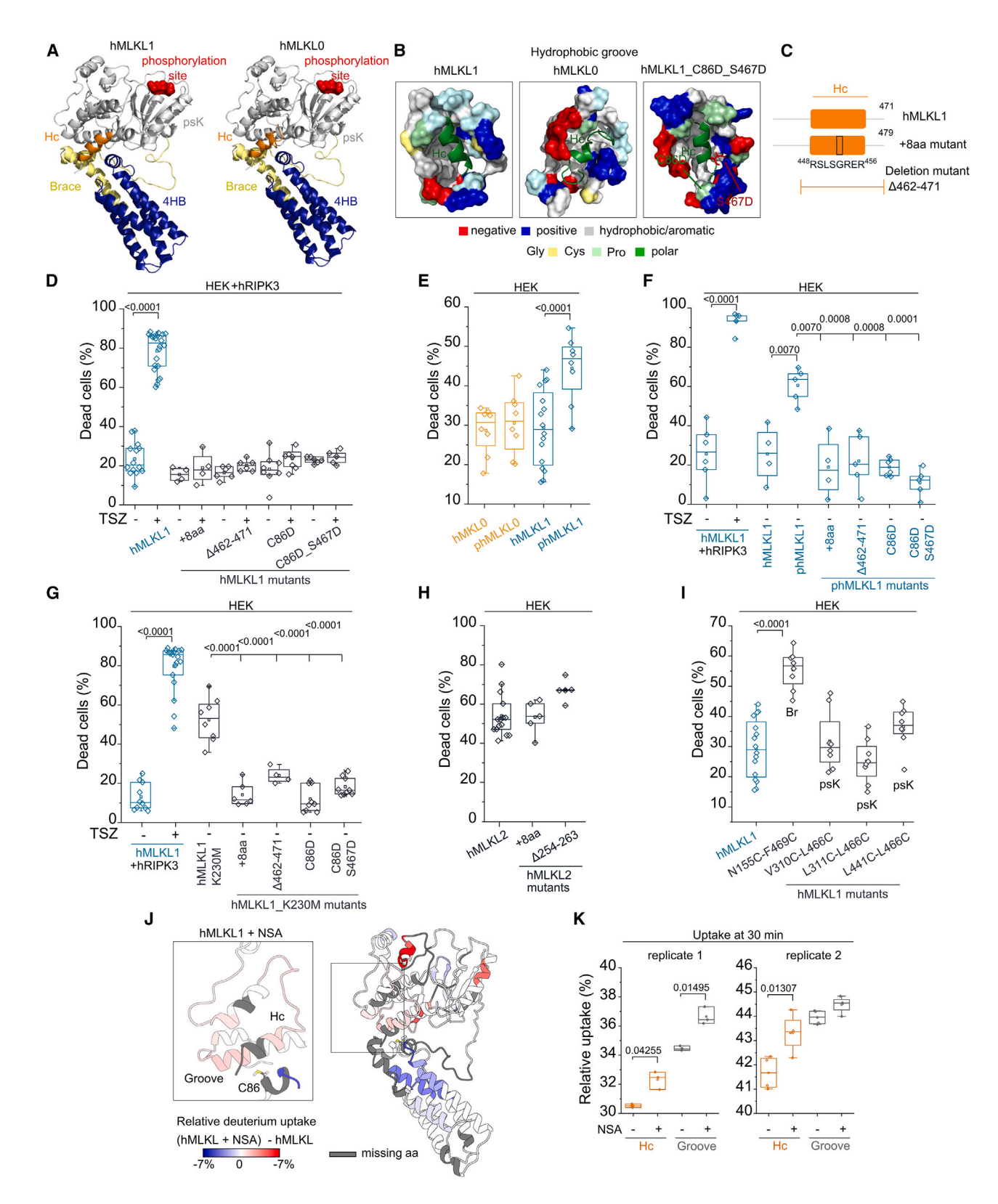


Figure 5. Hc into groove interaction is also essential for hMLKL

(A) Models of the 3D structure of hMLKL1 and hMLKL0.

(B) Hydrophobic groove of hMLKL1, hMLKL0 and the mutant hMLKL1_C86D_S467D.



and is required for necroptosis induction, placing Hc/groove interactions at the core of MLKL activation.

The Hc/groove interaction is evolutionarily conserved in human MLKL

Human MLKL is annotated as two isoforms (hMLKL1, UniProt: Q8NB16-1, hMLKL2, and UniProt: Q8NB16-2) with hMLKL2 lacking a major part of the psK domain³⁶ (Figures 4A and S5A). Our analysis of the human genome suggested the potential existence of an alternative splicing variant containing five additional amino acids in the Hc of hMLKL1 (here referred to as hMLKL0). In agreement with this, we detected hMLKL0 at mRNA level in WT A549 and HT-29 cells, and similar to hMLKL1, this variant was upregulated upon IFN stimulation (Figures 4B and 4C). Specific peptides of hMLKL0 were also found in WT HT-29 cells by mass spectrometry (Figures 4D and S5B), indicative of endogenous protein expression.

Functional characterization of the human isoforms showed that hMLKL0 was necroptosis deficient and that hMLKL1 could be activated upon TSZ treatment, while hMLKL2 was intrinsically active (Figures 4E and 4F), as reported. Furthermore, MLKL-/- HT-29 cells were desensitized to necroptosis when hMLKL0 was co-expressed with hMLKL1 compared with hMLKL1 alone (Figure 4G), while WT HT-29 cells were sensitized to necroptosis upon hMLKL0 knockdown (Figures 4D and 4H). These findings reveal the existence of an anti-necroptotic isoform of MLKL also in humans, hMLKL0, which functionally resembles mMLKL1, while hMLKL1 and hMLKL2 correspond to the mouse orthologs mMLKL2 and mMLKL3, respectively.

Structural models of hMLKL0 and hMLKL1 refined by MD simulations (Figure 5A) suggested that the Hc of hMLKL1 also accommodated in a hydrophobic groove, mediating interdomain interactions with the 4HB and the Br. In contrast, the Hc/groove was disrupted in hMLKL0 (Figures 5B and S5C). MD simulations of their phosphomimetic versions³⁷ suggested structure stabilization leading to remodeling of Hc/groove interactions and Br stabilization in phMLKL1 but not in phMLKL0 (Figures S5D–S5G).

These predictions guided experiments showing that either insertion of an extra sequence, deletion of the C terminus, or mutations disrupting Hc/groove interaction completely abrogated the activity of hMLKL1 without affecting protein levels (Figures 5B-5D, S5C, and S5H-S5K). Exchanging Cys86 with Asp at the hydrophobic groove of hMLKL1 (either alone or together with Ser467 in the Hc) also disrupted Hc/groove interactions in MD simulations and abolished its activity experimentally without altering expression levels or phos-

phorylation (Figures S5H–S5K). Similar to mouse MLKL, phosphomimetic hMLKL0 remained inactive, supporting that insertion of a short amino acid sequence in the Hc is dominant over phosphorylation to prevent MLKL activation (Figure 5E). Accordingly, Hc/groove destabilization hindered the activity of the intrinsically active mutants hMLKL1_T357E_S358D and hMLKL1_K230M^{37,38} (Figures 5F and 5G), while the activity of hMLKL2 lacking the psK domain was not affected by alterations in the Hc (Figure 5H). Stabilization of Hc/groove interactions through S–S bonds turned MLKL intrinsically active (Figure 5I). These results demonstrate that the key role of the Hc/groove interaction is conserved between mouse and human MLKL, despite their inter-species structural differences.

Cys86, the residue targeted by the covalent MLKL inhibitor necrosulfonamide (NSA), is located in the hydrophobic groove. According to our structural model of Hc/grove interaction, we reasoned that NSA binding would induce groove opening and displacement of the Hc, making it more accessible to the solvent. To test this, we performed hydrogen-deuterium exchange mass spectrometry (HDX-MS) of hMLKL1 upon incubation with NSA (Figures 5J, 5K, S5L, and S5M) and detected an increase in deuterium uptake for peptides covering the Hc and the adjacent region of the groove. The collective evidence from orthogonal methods strongly supports our structural model, which positions Hc insertion into the hydrophobic groove as a key step required for MLKL activation.

The Hc/groove interaction of MLKL can be selectively targeted by small molecules to inhibit necroptosis

By in silico screening, we selected MBA-h1 and MBA-m1 as putative inhibitors that target the Hc/groove of human and mouse MLKL, respectively (Figures 6A and 6B). MBA-h1 inhibited necroptosis in human WT HT-29 (Figure S6A) and HeLa-hRIPK3 knockin cells in a dose-dependent manner (Figures 6C and 6D), while MBA-m1 delayed necroptosis in mouse WT NIH-3T3 cells (Figures 6E and 6F). In contrast to the covalent inhibitors of human MLKL, NSA, and BI-8925, MBA-h1 and MBA-m1 delayed the kinetics of cell death (Figure S6B). This kinetic effect might be the consequence of the non-covalent targeting of MLKL by MBAs, thereby acting as reversible inhibitors. While MBA-h1 was less potent than the classic necroptotic inhibitors Nec1s (RIPK1) and GSK'872 (RIPK3) in human cells, MBA-m1 was as effective as Nec1s in mouse cells (Figure S6B).

MBA-h1 inhibited necroptosis in $MLKL^{-/-}$ HT-29 cells re-expressing hMLKL1, and MBA-m1 had the same effect in $Mlkl^{-/-}$ NIH-3T3 cells re-expressing mMLKL2 (Figure S6C). MBA-h1 was not toxic at the highest tested concentration (100 μ M) (Figures 6C and S6A), while we detected MBA-m1 toxicity above

⁽C) Insertion and deletion mutants of hMLKL1. aa: amino acids.

⁽D-I) Necroptotic activity of HEK cells transfected with indicated GFP-tagged versions of hMLKL1. (D) Hc/groove mutants of hMLKL1. (E) phosphomimetic mutants (T357E/S358D) of hMLKL0 and hMLKL1. Hc/groove mutations on hMLKL1_T357E/S358D (F), intrinsically active mutant hMLKL1_K230M (G) or hMLKL2 (H). (I) Double Cys mutants at the indicated positions within the Hc/groove.

⁽J and K) Differential deuterium exchange during binding of NSA to hMLKL1 after 30 min of labeling. (J) Ribbon representation of hMLKL1 colored according to accessibility based on deuterium exchange. (K) Relative deuterium uptake values obtained from curves shown in Figure S5L, after 30 min of labeling. Data in (K) correspond to values from two independent biological replicates containing at least three technical replicates each.

Dots correspond to individual replicates and whiskers ranges correspond to the SD. p values for statistically significant comparisons are shown. See also Figure S5.



MBA-m1 (B).



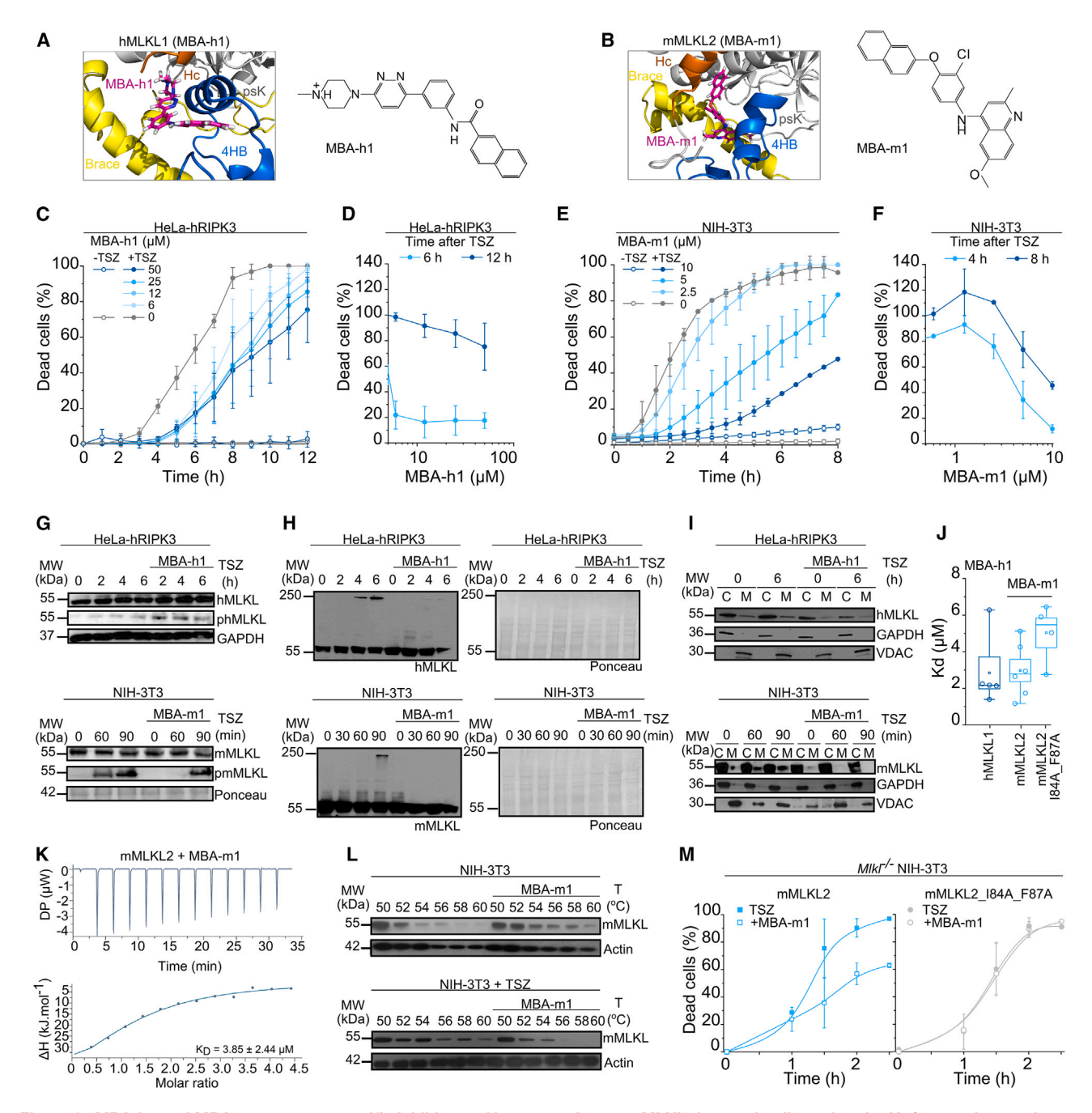


Figure 6. MBA-h1 and MBA-m1 are new specific inhibitors of human and mouse MLKL that act by disrupting the Hc/groove interaction (A and B) Models of the 3D structure of hMLKL1-MBA-h1 complex and chemical structure of MBA-h1 (A) or mMLKL2-MBA-m1 complex and chemical structure of

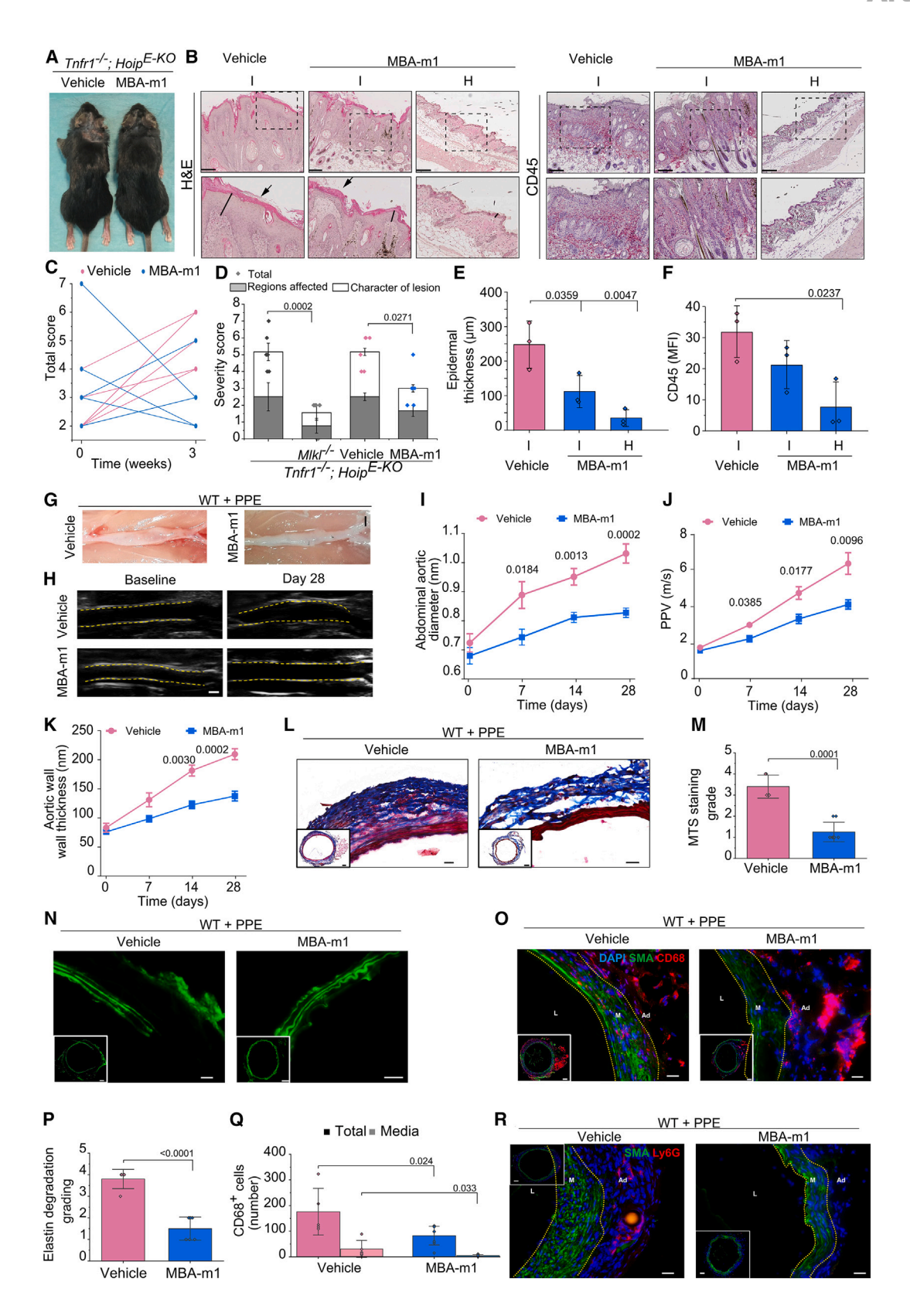
(C–F) Inhibitory effect of MBA-h1 and MBA-m1 on necroptotic cell death. Kinetics of cell death in human HeLa-hRIPK3 (C) or mouse WT NIH-3T3 cells (E). Dose dependence of the inhibitory effect in HeLa-hRIPK3 (D) or WT NIH-3T3 cells (F).

- (G-I) Effect of the inhibitors on MLKL phosphorylation (G), oligomerization (H), and membrane translocation (I). Samples were processed under reducing in (G) and (I) or non-reducing conditions in (H), and analyzed by WB. C, cytosolic fraction; M, membrane fraction.
- (J) Dissociation constant (Kd) values of the interaction of the indicated recombinant MLKL and the inhibitors.
- (K) ITC curves, obtained for the titration of recombinant mMLKL2 with different amounts of MBA-m1.
- (L) Effect of MBA-m1 on the thermal stability of MLKL in cells. WT NIH-3T3 cells were treated or not with 10 μM MBA-m1 in the absence (top) or the presence (bottom) of TSZ.

(M) Inhibitory effect of 10 μM MBA-m1 in MIkl^{-/-} NIH-3T3 cells transfected with mMLKL2_GFP or the mutant mMLKL2_I84A_F87A-GFP.

Data in (C)–(F) and (M) are shown as main values \pm SD. In (J) and (K), dots correspond to individual values and whiskers ranges to the SD. See also Figures S6 and S7.





(legend on next page)

Article



 $10\,\mu\text{M}$ (Figure S6D). MBA-m1 delayed phosphorylation of mouse MLKL, which appeared 90 min after TSZ treatment, a condition under which strong inhibition of cell death was still observed (Figures 6E and 6G). Yet, MBA-m1 did not affect RIPK3:MLKL interaction upon TSZ treatment (Figure S6E). These results suggest that MBA-m1 can inhibit MLKL-mediated necroptosis after its phosphorylation, discarding interference with the activity of upstream RIPK1 and RIPK3. MBA-h1 did not block this process in human cells, also discarding an effect on RIPK1/3 (Figures 6G and S6F). Moreover, both inhibitors interfered with MLKL oligomerization and translocation to membranes (Figures 6H, 6I, S6G, and S6H).

In support of specificity, the inhibitory effect of MBA-h1 and MBA-m1 was not observed in cells expressing the intrinsically active variants hMLKL2 and mMLKL3, respectively, which lack the groove binding site (Figure S7A), or when the human MLKL inhibitor was tested in mouse cells and vice versa (Figures S7B and S7C). The binding affinity of MBA-h1 to hMLKL1 and of MBA-m1 to mMLKL2 was in the low μM range, as determined by microscale thermophoresis (MST) (Figures 6J and S7D). Each inhibitor delayed the kinetics of vesicle permeabilization induced by the corresponding MLKL ortholog (Figures S7E–S7G).

We confirmed the physical interaction of MBA-m1 with mMLKL2 *in vitro* by isothermal titration calorimetry (ITC) (Figure 6K) and cellular thermal shift assay (CETSA) (Figures 6L and S7H). As additional proof of specificity in the cellular context, we rationally designed mutations that affected the interaction of MBA-m1 with mMLKL2 without altering its necroptosis activity. The mutant mMLKL2_I84A_F87A, with reduced affinity for MBA-m1 (Figures 6J and S7D), but unaffected necroptosis-inducing capacity, was inert to inhibition by MBA-m1 in cell death assays (Figure 6M). Moreover, MBA-m1 did not alter the thermal stability of RIPK1 or RIPK3 (Figures S7I and S7J), and it did not affect RIPK1-mediated apoptosis either in WT or in *MIKI*^{-/-} NIH-3T3 cells (Figure S7K). Altogether, these results strongly indicate that the effect of MBA-m1 on cell death is due to its action on mMLKL2 and not to off-target effects.

Finally, we assessed the efficacy of MBA-m1 *in vivo*. For this, we selected animal models of necroptosis that were demonstrated to be MLKL dependent. Keratinocyte-specific absence of the linear ubiquitin chain assembly complex (LUBAC) component heme-oxidized iron regulatory protein 2 ubiquitin ligase 1 (HOIL-1)-interacting protein (HOIP) (*Hoip*^{E-KO}) combined with

constitutive tumor necrosis factor receptor 1 (TNFR1) deficiency (*Tnfr1*^{-/-}) induces fatal dermatitis, which is reverted by loss of MLKL.⁵ Treatment with MBA-m1 significantly ameliorated dermatitis as assessed by severity scoring of macroscopic lesions and histological examination (Figures 7A–7F). MBA-m1-treated mice showed patches of healthy and moderately inflamed regions in the dorsal skin, whereas mice treated with a vehicle suffered from skin inflammation throughout the dorsal skin (Figures 7A and 7B). Accordingly, treated mice presented decreased infiltration by CD45-positive cells when healthy and inflamed tissue were compared (Figure 7F).

To gather further evidence of the ability of MBA-m1 to improve necroptosis-driven disease *in vivo*, we additionally tested its efficacy in a mouse model of abdominal aortic aneurysm disease.³⁹ Remarkably, animals treated with MBA-m1 showed attenuation of aortic diameter increase as assessed by ultrasound analysis when compared with control mice (Figures 7G-7K). Masson's trichrome staining (MTS) and elastin fluorescence imaging showed that aortic structural alterations were ameliorated in MBA-m1-treated mice. MLKL inhibition also reduced the infiltration of immune cells (Figures 7L-7Q). Mice treated with MBA-m1 harbored significantly lower counts of CD68⁺ macrophages and Ly6G⁺ myeloid cells compared with those treated with vehicle (Figure 7R).

Altogether these results suggest that inhibiting MLKL activity by interfering with the Hc/groove interaction can be achieved in vivo and that this treatment prevents the progression of necroptosis-driven pathologies.

DISCUSSION

Here, we reveal how MLKL structure regulates function based on the drastic effect of ostensibly minor sequence divergence between two isoforms of MLKL. The presence of just a few extra amino acids in the Hc unexpectedly alters the molecular behavior and abrogates the death-inducing activity of mouse and human MLKL. The expression of the suppressive MLKL isoform is regulated by inflammatory cues and is conserved in humans and mice. Both MLKL isoforms counterbalance each other to modulate necroptosis sensitivity, which may play a role in fine-tuning the level of necroptosis-induced inflammation in response to gram-negative bacterial infection or other MLKL-associated diseases.

Figure 7. MBA-m1 ameliorates disease in mouse models of MLKL-driven dermatitis and abdominal aortic aneurysm

(A–F) Effect of MBA-m1 on *Tnfr1*^{-/-};*Hoip*^{E-KO} mice suffering dermatitis. (A) Representative images of skin lesions. (B) Microscopic characterization. Left: representative images showing the alterations in the epidermal layer (black line) and hyperkeratosis (arrow). H&E: haemotoxylin and eosin staining. Right: representative images showing the immunohistochemistry with a pan-immune marker, CD45 (red staining). I, inflamed tissue; H, healthy tissue. Scale bar: 200 μm. (C) Dermatitis progression in individual mice. (D) average scoring of skin lesions at endpoint. Statistics: two-way ANOVA with Sidak's multiple comparisons tests. (E) Quantification of epidermal thickness. (F) CD45 intensity. MFI, mean fluorescence intensity. Statistics: one-way ANOVA with Tukey's multiple comparisons tests. Dots correspond to values obtained from individual mice.

(G–R) Effect of MBA-m1 on porcine pancreatic elastase (PPE)-operated mice. (G) Representative macrographs. (H) Representative ultrasound images of abdominal aorta. Scale bar: 1 mm. (I) Absolute diameters of infrarenal aortic segments determined from ultrasonic images. (J) Pulse propagation velocity (PPV). (K) Aortic wall thickness. (L) Representative macroscopic images from Masson's trichrome staining (MTS). (M) Grading for the MTS staining. (N) Representative elastin autofluorescence images. (O) Representative confocal images of smooth muscle cell marker (SMA) (green) and CD68 (red). (P) Grading of elastin degradation. (Q) Number of CD68⁺ cells from total and cells only in media. (R) Representative confocal images of SMA (green) and Ly6G (red). In (L), (N), (O), and (R), scale bars: 100 and 20 μm, M, media and Ad, adventitia. In (I)–(K), (M), (P), and (Q), statistics: unpaired two-tailed t test.

Dots in (C)–(F), (M), (P), and (Q) correspond to individual animals. Bar plots and data in (E), (F), and (I)–(K) are shown as main values \pm SD. p values for statistically significant comparisons are shown.



These findings shift our understanding of MLKL-driven necroptosis, whose biological net-effects result from the antagonistic interaction between isoforms with different biological roles that control cell death. While mMLKL2 exerts the cell death effector function, mMLKL1 represents a natural suppressor of necroptosis that can interact with mMLKL2 and restrict its activation. As a result, the splice-dependent insertion of a short amino acid sequence in the Hc of MLKL generates an isoform with an altered protein interaction network that diverges functionally from the necroptosis-inducing activity. Besides the typical trait of pseudokinases in regulating the function of complex assemblies in cellular pathways, 40 modulation of the necroptotic signaling axis through alternative splicing of MLKL enhances the complexity and versatility of the regulatory network.³² Therefore, our discoveries open research avenues regarding the physiological relevance and precise mechanism of how MLKL variants control cellular responses to environmental changes.

Our findings support a model for the molecular mechanism of mMLKL1 that is compatible with its sub-stoichiometric expression levels relative to mMLKL2. We discover a positive feedback mechanism by which mMLKL2, but not mMLKL1, promotes the enzymatic activity of the necrosome. The anti-necroptotic activity of mMLKL1 depends on protein/protein interaction surfaces. While it can interact with itself, with mMLKL2 and, to a lower extent, with RIPK3, mMLKL1 can also reduce the interaction of mMLKL2 with RIPK3. Proper assembly of RIPK3 molecules into supramolecular fibers seems to be essential for the formation of the functional necrosome.²¹ Our data support a model in which mMLKL2 can specifically amplify the enzymatic activity of the necrosome, likely by promoting its functional supramolecular assembly. mMLKL1 would then act as a poison and hamper this positive feedback, having a strong impact on necroptosis sensitivity (Figure 2M).

Our results shed light on the functional impact of alternative splicing of microexons in cells, which are highly conserved very short exons (3–27 nucleotides) whose biological functions remain poorly understood. They have been shown to be critical for neuronal development and function⁴¹ and to play a role in pancreatic islet function and glucose homeostasis.⁴² Our findings add an unrecognized function for microexons in cell death regulation by showing how this mechanism generates an MLKL isoform that diverges from the canonical function and that regulates necroptosis sensitivity.

We also report on the discovery of a previously unrecognized core mechanism of MLKL activation conserved between mouse and human orthologs: the Hc α -helix is essential for MLKL activation, in line with a model in which its accommodation into a hydrophobic groove is required for its necroptotic function. Alteration of Hc folding would hinder the assembly of the groove and the stabilization of the active conformation. This challenges the current paradigm for MLKL auto-regulation that considers the psK exclusively as an inhibitor of the killer 4HB. 17,43,44 Therefore, our results reveal Hc as a key structural element that regulates MLKL activity dominant over phosphorylation and that can be exploited therapeutically.

Our discovery of this druggable site in MLKL, based on the knowledge gained through the structure-function analysis of the isoforms, opens a strategy to develop binders of MLKL that inhibit its necroptotic activity via non-covalent interactions, without interfering with upstream signals. MBA-m1 and MBA-h1 are proof-of-concept compounds of insufficient potency to undergo clinical trials. Yet, medicinal chemistry optimization holds promise to guide the development of improved compounds targeting human MLKL via the same strategy for the treatment of necroptosis-related diseases.

Limitations of the study

While our results uncover the critical role of the Hc/groove interaction for MLKL activity, it is still unclear whether this interaction takes place in cis or in trans. Also, the molecular determinants driving the higher tendency of mMLKL1 to oligomerize and interact with membranes, as well as its lack of phosphorylation, remain unclear. Dissecting the structural basis of these differences will likely require atomic-resolution analysis, which so far remains elusive, likely due to aggregation/oligomerization issues. Our data suggest that mMLKL1 can interfere with mMLKL2 activity by acting as a poison for the necrosome. However, at this point we cannot distinguish whether this function is exerted via sequestration of mMLKL2 into necroptosis-deficient complexes, or by directly interfering with the necrosome supramolecular assembly. The question about how active MLKL mediates a positive feedback loop promoting RIPK3 phosphorylation and necrosome activity remains unanswered and addressing it will require the development of more advanced tools. Finally, the MLKL inhibitors characterized here represent proof-of-concept molecules still in an early phase of drug development and will require several rounds of optimization before they can become drug candidates. Although our results support on-target effects on MLKL, further work will be required to define potential offtarget binding partners.

RESOURCE AVAILABILITY

Lead contact

In case additional information stated in this article is needed, please refer to the lead contact, Ana Garcia-Saez (ana.garcia@biophys.mpg.de).

Materials availability

For further information and requests about materials and resources used in this study, please refer to the lead contact.

Data and code availability

- All unprocessed blots and imaging data were deposited at Mendeley Data: https://doi.org/10.17632/c56wwg84sp.1. The deposited data of this study will be publicly available as of the date of publication.
- This paper does not report original code.
- Any additional information required to reanalyze the data reported in this
 paper is available from the lead contact upon request.

ACKNOWLEDGMENTS

This project was funded by the Deutsche Forschungsgesellschaft (DFG): GA1641/5-1 (418168917) and SFB1403 (414786233, subprojects A01, A02, A10, and B07) as well as the TRR259 (397484323, subproject B05) and the GoBio Initial program from the Bundesministerium für Bildung und Forschung (BMBF) (NEKIN). It was also partially supported by the Max Planck Society and the European Research Council (ERC-2012-StG-309966 and ERC-2019-CoG-817758). Further support was received by N.P. (SFB1399, 413326622, subproject A06), R.A.E. (Alexander von Humboldt Foundation),

Article



W.W.-L.W. (SNSF – 310030 159613), H.W. (Welcome Trust Investigator Award [214342/Z/18/Z] and a Medical Research Council grant [MR/S00811X/1]), and D.P.T. (Natural Sciences and Engineering Research Council, the Canada Research Chairs program, Compute Canada resources funded by the Canada Foundation for Innovation and partners). We thank Annika Sarembe, Sabine Schaefer, and Gudrun Zimmer for technical support and Prof. Andreas Villunger for helpful discussions.

AUTHOR CONTRIBUTIONS

Conceptualization, U.R., P.A.V., and A.J.G.-S.; methodology, L.W., S.M., M.A., H.W., M.M., M.P., and N.P.; investigation, U.R., V.M.-O., P.A.V., Y.A., M.G., R.S., S.Z., J.S., L.W., H.N.N., J.Z., H.L., Y.-G.C., M.I., K.K., L.V., P.B., R.A.E., S.M., V.A., and J.W.; resources, D.P.T., J.W., J.L., M.A., H.W., W.W.-L.W., G.L., M.M., M.P., and N.P.; writing – original draft, U.R. and A.J.G.-S.; writing – review and editing, V.M.-O., P.A.V., S.Z., L.W., R.A.E., H.W., M.P., and N.P.; visualization, U.R., V.M.-O., and P.A.V.; supervision and project administration, U.R. and A.J.G.-S.; and funding acquisition, U.R., M.A., and A.J.G.-S.

DECLARATION OF INTERESTS

A.J.G.-S., U.R., P.A.V., W.W.-L.W., H.W., and N.P. filed a patent application for an invention based on a method of modulating MLKL activity as well as for the molecules reported in the manuscript (patent application number is EP20173672.5).

STAR*METHODS

Detailed methods are provided in the online version of this paper and include the following:

- KEY RESOURCES TABLE
- EXPERIMENTAL MODEL AND STUDY PARTICIPANT DETAILS
 - Primary cells and cell lines
 - O Stable cell line generation
 - $\,\circ\,$ Animal breeding and organ isolation
 - Mouse generation
 - Mouse model of MLKL-dependent dermatitis
 - o Mouse model of MLKL-dependent abdominal aortic aneurysm
- METHOD DETAILS
 - o Generation of mouse and human MLKL mutants
 - Transient transfection
 - $_{\odot}\,$ Treatments to induce expression of MLKL
 - $\,\circ\,$ RNA isolation and RT-qPCR
 - Treatments for necroptosis induction
 - Flow cytometry assays
 - Incucyte experiments
 - Brightfield and confocal microscopy
 - o TIRF
 - Western blotting
 - Subcellular fractionation
 - o TUBE affinity precipitation
 - Cellular thermal shift assays
 - Co-immunoprecipitation assays
 - o Detection of human isoforms by mass spectrometry
 - Expression and purification of recombinant MLKL
 - HDX mass spectrometry
 - MST experiments
 - o ITC experiments
 - O Vesicle preparation and permeabilization assay
 - Analysis of Ripk1^{E-KO} samples
 - Macroscopic assessment of skin lesions
 - o Immunohistochemistry of skin samples
 - $_{\odot}\,$ Immunohistochemistry of abdominal aorta samples
 - Modeling the 3D structures of the full-length mouse and human MLKL isoforms

- o Molecular dynamics simulations
- Analysis of the MD simulations
- Structure-based virtual screening
- QUANTIFICATION AND STATISTICAL ANALYSIS

SUPPLEMENTAL INFORMATION

Supplemental information can be found online at https://doi.org/10.1016/j.molcel.2025.03.015.

Received: September 12, 2023 Revised: February 10, 2025 Accepted: March 17, 2025 Published: April 9, 2025

REFERENCES

- Pasparakis, M., and Vandenabeele, P. (2015). Necroptosis and its role in inflammation. Nature 517, 311–320. https://doi.org/10.1038/nature14191.
- 2. Newton, K., and Manning, G. (2016). Necroptosis and Inflammation. Annu. Rev. Biochem. 85, 743–763. https://doi.org/10.1146/annurev-biochem-060815-014830
- Jiao, H., Wachsmuth, L., Kumari, S., Schwarzer, R., Lin, J., Eren, R.O., Fisher, A., Lane, R., Young, G.R., Kassiotis, G., et al. (2020). Z-nucleicacid sensing triggers ZBP1-dependent necroptosis and inflammation. Nature 580, 391–395. https://doi.org/10.1038/s41586-020-2129-8.
- Schwarzer, R., Jiao, H., Wachsmuth, L., Tresch, A., and Pasparakis, M. (2020). FADD and Caspase-8 Regulate Gut Homeostasis and Inflammation by Controlling MLKL- and GSDMD-Mediated Death of Intestinal Epithelial Cells. Immunity 52, 978–993.e6. https://doi.org/10.1016/j.immuni.2020.04.002.
- Taraborrelli, L., Peltzer, N., Montinaro, A., Kupka, S., Rieser, E., Hartwig, T., Sarr, A., Darding, M., Draber, P., Haas, T.L., et al. (2018). LUBAC prevents lethal dermatitis by inhibiting cell death induced by TNF, TRAIL and CD95L. Nat. Commun. 9, 3910. https://doi.org/10.1038/s41467-018-0615-8
- Müller, T., Dewitz, C., Schmitz, J., Schröder, A.S., Bräsen, J.H., Stockwell, B.R., Murphy, J.M., Kunzendorf, U., and Krautwald, S. (2017). Necroptosis and ferroptosis are alternative cell death pathways that operate in acute kidney failure. Cell. Mol. Life Sci. 74, 3631–3645. https://doi.org/10. 1007/s00018-017-2547-4.
- Zhou, T., Wang, Q., Phan, N., Ren, J., Yang, H., Feldman, C.C., Feltenberger, J.B., Ye, Z., Wildman, S.A., Tang, W., et al. (2019). Identification of a novel class of RIP1/RIP3 dual inhibitors that impede cell death and inflammation in mouse abdominal aortic aneurysm models. Cell Death Dis. 10, 226. https://doi.org/10.1038/s41419-019-1468-6.
- Seehawer, M., Heinzmann, F., D'Artista, L., Harbig, J., Roux, P.F., Hoenicke, L., Dang, H., Klotz, S., Robinson, L., Doré, G., et al. (2018). Necroptosis microenvironment directs lineage commitment in liver cancer. Nature 562, 69–75. https://doi.org/10.1038/s41586-018-0519-y.
- Ofengeim, D., Mazzitelli, S., Ito, Y., DeWitt, J.P., Mifflin, L., Zou, C., Das, S., Adiconis, X., Chen, H., Zhu, H., et al. (2017). RIPK1 mediates a diseaseassociated microglial response in Alzheimer's disease. Proc. Natl. Acad. Sci. USA 114, E8788–E8797. https://doi.org/10.1073/pnas.1714175114.
- Lalaoui, N., Boyden, S.E., Oda, H., Wood, G.M., Stone, D.L., Chau, D., Liu, L., Stoffels, M., Kratina, T., Lawlor, K.E., et al. (2020). Mutations that prevent caspase cleavage of RIPK1 cause autoinflammatory disease. Nature 577, 103–108. https://doi.org/10.1038/s41586-019-1828-5.
- Kaiser, W.J., Sridharan, H., Huang, C., Mandal, P., Upton, J.W., Gough, P.J., Sehon, C.A., Marquis, R.W., Bertin, J., and Mocarski, E.S. (2013).
 Toll-like receptor 3-mediated necrosis via TRIF, RIP3, and MLKL. J. Biol. Chem. 288, 31268–31279. https://doi.org/10.1074/jbc.M113.462341.
- 12. Zhang, T., Yin, C., Boyd, D.F., Quarato, G., Ingram, J.P., Shubina, M., Ragan, K.B., Ishizuka, T., Crawford, J.C., Tummers, B., et al. (2020).



- Influenza Virus Z-RNAs Induce ZBP1-Mediated Necroptosis. Cell 180, 1115–1129.e13. https://doi.org/10.1016/j.cell.2020.02.050.
- Upton, J.W., and Kaiser, W.J. (2017). DAI Another Way: Necroptotic Control of Viral Infection. Cell Host Microbe 21, 290–293. https://doi.org/ 10.1016/j.chom.2017.01.016.
- Sun, L., Wang, H., Wang, Z., He, S., Chen, S., Liao, D., Wang, L., Yan, J., Liu, W., Lei, X., et al. (2012). Mixed lineage kinase domain-like protein mediates necrosis signaling downstream of RIP3 kinase. Cell 148, 213–227. https://doi.org/10.1016/j.cell.2011.11.031.
- Samson, A.L., Garnish, S.E., Hildebrand, J.M., and Murphy, J.M. (2021). Location, location, location: A compartmentalized view of TNF-induced necroptotic signaling. Sci. Signal. 14, eabc6178. https://doi.org/10. 1126/scisignal.abc6178.
- Murphy, J.M., Czabotar, P.E., Hildebrand, J.M., Lucet, I.S., Zhang, J.G., Alvarez-Diaz, S., Lewis, R., Lalaoui, N., Metcalf, D., Webb, A.I., et al. (2013). The pseudokinase MLKL mediates necroptosis via a molecular switch mechanism. Immunity 39, 443–453. https://doi.org/10.1016/j.immuni.2013.06.018.
- Hildebrand, J.M., Tanzer, M.C., Lucet, I.S., Young, S.N., Spall, S.K., Sharma, P., Pierotti, C., Garnier, J.M., Dobson, R.C.J., Webb, A.I., et al. (2014). Activation of the pseudokinase MLKL unleashes the four-helix bundle domain to induce membrane localization and necroptotic cell death. Proc. Natl. Acad. Sci. USA 111, 15072–15077. https://doi.org/10. 1073/pnas.1408987111.
- Petrie, E.J., Birkinshaw, R.W., Koide, A., Denbaum, E., Hildebrand, J.M., Garnish, S.E., Davies, K.A., Sandow, J.J., Samson, A.L., Gavin, X., et al. (2020). Identification of MLKL membrane translocation as a checkpoint in necroptotic cell death using Monobodies. Proc. Natl. Acad. Sci. USA 117, 8468–8475. https://doi.org/10.1073/pnas.1919960117.
- Chen, X., Li, W., Ren, J., Huang, D., He, W.T., Song, Y., Yang, C., Li, W., Zheng, X., Chen, P., et al. (2014). Translocation of mixed lineage kinase domain-like protein to plasma membrane leads to necrotic cell death. Cell Res. 24, 105–121. https://doi.org/10.1038/cr.2013.171.
- Garnish, S.E., Meng, Y., Koide, A., Sandow, J.J., Denbaum, E., Jacobsen, A.V., Yeung, W., Samson, A.L., Horne, C.R., Fitzgibbon, C., et al. (2021). Conformational interconversion of MLKL and disengagement from RIPK3 precede cell death by necroptosis. Nat. Commun. 12, 2211. https://doi.org/10.1038/s41467-021-22400-z.
- Chen, X., Zhu, R., Zhong, J., Ying, Y., Wang, W., Cao, Y., Cai, H., Li, X., Shuai, J., and Han, J. (2022). Mosaic composition of RIP1–RIP3 signalling hub and its role in regulating cell death. Nat. Cell Biol. 24, 471–482. https:// doi.org/10.1038/s41556-022-00854-7.
- Espiritu, R.A., Pedrera, L., and Ros, U. (2019). Tuning the way to die: implications of membrane perturbations in necroptosis. Adv. Biomembr. Lipid Self-Assembly 29, 201–247. https://doi.org/10.1016/bs.abl.2019.01.006.
- Khoury, M.K., Gupta, K., Franco, S.R., and Liu, B. (2020). Necroptosis in the Pathophysiology of Disease (Elsevier Inc.). https://doi.org/10.1016/j. ajpath.2019.10.012.
- Peltzer, N., and Walczak, H. (2019). Cell Death and Inflammation A Vital but Dangerous Liaison. Trends Immunol. 40, 387–402. https://doi.org/10. 1016/j.it.2019.03.006.
- Mandal, P., Berger, S.B., Pillay, S., Moriwaki, K., Huang, C., Guo, H., Lich, J.D., Finger, J., Kasparcova, V., Votta, B., et al. (2014). RIP3 Induces Apoptosis Independent of Pronecrotic Kinase Activity. Mol. Cell 56, 481–495. https://doi.org/10.1016/j.molcel.2014.10.021.
- Pierotti, C.L., Tanzer, M.C., Jacobsen, A.V., Hildebrand, J.M., Garnier, J.M., Sharma, P., Lucet, I.S., Cowan, A.D., Kersten, W.J.A., Luo, M.X., et al. (2020). Potent Inhibition of Necroptosis by Simultaneously Targeting Multiple Effectors of the Pathway. ACS Chem. Biol. 15, 2702– 2713. https://doi.org/10.1021/acschembio.0c00482.
- 27. Yan, B., Liu, L., Huang, S., Ren, Y., Wang, H., Yao, Z., Li, L., Chen, S., Wang, X., and Zhang, Z. (2017). Discovery of a new class of highly potent necroptosis inhibitors targeting the mixed lineage kinase domain-like pro-

- tein. Chem. Commun. (Camb) 53, 3637–3640. https://doi.org/10.1039/c7cc00667e.
- Dannappel, M., Vlantis, K., Kumari, S., Polykratis, A., Kim, C., Wachsmuth, L., Eftychi, C., Lin, J., Corona, T., Hermance, N., et al. (2014). RIPK1 maintains epithelial homeostasis by inhibiting apoptosis and necroptosis. Nature 513, 90–94. https://doi.org/10.1038/nature13608.
- Liu, Z., Dagley, L.F., Shield-Artin, K., Young, S.N., Bankovacki, A., Wang, X., Tang, M., Howitt, J., Stafford, C.A., Nachbur, U., et al. (2021).
 Oligomerization-driven MLKL ubiquitylation antagonizes necroptosis.
 EMBO J. 40, e103718. https://doi.org/10.15252/embj.2019103718.
- Garcia, L.R., Tenev, T., Newman, R., Haich, R.O., Liccardi, G., John, S.W., Annibaldi, A., Yu, L., Pardo, M., Young, S.N., et al. (2021). Ubiquitylation of MLKL at lysine 219 positively regulates necroptosis-induced tissue injury and pathogen clearance. Nat. Commun. 12, 3364. https://doi.org/10. 1038/s41467-021-23474-5.
- Davies, K.A., Tanzer, M.C., Griffin, M.D.W., Mok, Y.F., Young, S.N., Qin, R., Petrie, E.J., Czabotar, P.E., Silke, J., and Murphy, J.M. (2018). The brace helices of MLKL mediate interdomain communication and oligomerisation to regulate cell death by necroptosis. Cell Death Differ. 25, 1567– 1580. https://doi.org/10.1038/s41418-018-0061-3.
- Ellis, J.D., Barrios-Rodiles, M., Çolak, R., Irimia, M., Kim, T.H., Calarco, J.A., Wang, X., Pan, Q., O'Hanlon, D., Kim, P.M., et al. (2012). Tissue-Specific Alternative Splicing Remodels Protein-Protein Interaction Networks. Mol. Cell 46, 884–892. https://doi.org/10.1016/j.molcel.2012. 05.037.
- Arnež, K.H., Kindlova, M., Bokil, N.J., Murphy, J.M., Sweet, M.J., and Gunčar, G. (2015). Analysis of the N-terminal region of human MLKL, as well as two distinct MLKL isoforms, reveals new insights into necroptotic cell death. Biosci. Rep. 36, e00291. https://doi.org/10.1042/BSR20150246.
- Tanzer, M.C., Matti, I., Hildebrand, J.M., Young, S.N., Wardak, A., Tripaydonis, A., Petrie, E.J., Mildenhall, A.L., Vaux, D.L., Vince, J.E., et al. (2016). Evolutionary divergence of the necroptosis effector MLKL. Cell Death Differ. 23, 1185–1197. https://doi.org/10.1038/cdd.2015.169.
- Rodriguez, D.A., Weinlich, R., Brown, S., Guy, C., Fitzgerald, P., Dillon, C.P., Oberst, A., Quarato, G., Low, J., Cripps, J.G., et al. (2016). Characterization of RIPK3-mediated phosphorylation of the activation loop of MLKL during necroptosis. Cell Death Differ. 23, 76–88. https://doi.org/10.1038/cdd.2015.70.
- Zhao, J., Jitkaew, S., Cai, Z., Choksi, S., Li, Q., Luo, J., and Liu, Z.G. (2012).
 Mixed lineage kinase domain-like is a key receptor interacting protein 3 downstream component of TNF-induced necrosis. Proc. Natl. Acad. Sci. USA 109, 5322–5327. https://doi.org/10.1073/pnas.1200012109.
- Wang, H., Sun, L., Su, L., Rizo, J., Liu, L., Wang, L.F., Wang, F.S., and Wang, X. (2014). Mixed Lineage Kinase Domain-like Protein MLKL Causes Necrotic Membrane Disruption upon Phosphorylation by RIP3. Mol. Cell 54, 133–146. https://doi.org/10.1016/j.molcel.2014.03.003.
- Yoon, S., Kovalenko, A., Bogdanov, K., and Wallach, D. (2017). MLKL, the Protein that Mediates Necroptosis, Also Regulates Endosomal Trafficking and Extracellular Vesicle Generation. Immunity 47, 51–65.e7. https://doi. org/10.1016/j.immuni.2017.06.001.
- Nemade, H., Mehrkens, D., Lottermoser, H., Yilmaz, Z.E., Picard, F.R., Hof, A., Schwab, G., Schelemei, P., Geißen, S., Guthoff, H., Sachinidis, A., et al. (2022). Inhibition of MLKL impairs abdominal aortic aneurysm development by attenuating smooth muscle cell necroptosis. Prepint at. bioRxiv. https://doi.org/10.1101/2022.11.24.517638.
- Tomoni, A., Lees, J., Santana, A.G., Bolanos-Garcia, V.M., and Bastida, A. (2019). Pseudokinases: From allosteric regulation of catalytic domains and the formation of macromolecular assemblies to emerging drug targets. Catalysts 9, 778. https://doi.org/10.3390/catal9090778.
- Irimia, M., Weatheritt, R.J., Ellis, J.D., Parikshak, N.N., Gonatopoulos-Pournatzis, T., Babor, M., Quesnel-Vallières, M., Tapial, J., Raj, B., O'Hanlon, D., et al. (2014). A highly conserved program of neuronal microexons is misregulated in autistic brains. Cell 159, 1511–1523. https://doi.org/10.1016/j.cell.2014.11.035.

Article



- Juan-Mateu, J., Bajew, S., Miret-Cuesta, M., Íñiguez, L.P., Lopez-Pascual, A., Bonnal, S., Atla, G., Bonàs-Guarch, S., Ferrer, J., Valcárcel, J., et al. (2023). Pancreatic microexons regulate islet function and glucose homeostasis. Nat. Metab. 5, 219–236. https://doi.org/10.1038/s42255-022-00734-2.
- Su, L., Quade, B., Wang, H., Sun, L., Wang, X., and Rizo, J. (2014). A plug release mechanism for membrane permeation by MLKL. Structure 22, 1489–1500. https://doi.org/10.1016/j.str.2014.07.014.
- Petrie, E.J., Sandow, J.J., Jacobsen, A.V., Smith, B.J., Griffin, M.D.W., Lucet, I.S., Dai, W., Young, S.N., Tanzer, M.C., Wardak, A., et al. (2018). Conformational switching of the pseudokinase domain promotes human MLKL tetramerization and cell death by necroptosis. Nat. Commun. 9, 2422. https://doi.org/10.1038/s41467-018-04714-7.
- Moerke, C., Bleibaum, F., Kunzendorf, U., and Krautwald, S. (2019). Combined Knockout of RIPK3 and MLKL Reveals Unexpected Outcome in Tissue Injury and Inflammation. Front. Cell Dev. Biol. 7, 19. https://doi. org/10.3389/fcell.2019.00019.
- Gong, Y.N., Guy, C., Olauson, H., Becker, J.U., Yang, M., Fitzgerald, P., Linkermann, A., and Green, D.R. (2017). ESCRT-III Acts Downstream of MLKL to Regulate Necroptotic Cell Death and Its Consequences. Cell 169, 286–300.e16. https://doi.org/10.1016/j.cell.2017.03.020.
- Lafont, E., Draber, P., Rieser, E., Reichert, M., Kupka, S., de Miguel, D., Draberova, H., von Mässenhausen, A., Bhamra, A., Henderson, S., et al. (2018). TBK1 and IKKε prevent TNF-induced cell death by RIPK1 phosphorylation. Nat. Cell Biol. 20, 1389–1399. https://doi.org/10.1038/s41556-018-0229-6.
- Peltzer, N., Rieser, E., Taraborrelli, L., Draber, P., Darding, M., Pernaute, B., Shimizu, Y., Sarr, A., Draberova, H., Montinaro, A., et al. (2014). HOIP deficiency causes embryonic lethality by aberrant TNFR1-mediated endothelial cell death. Cell Rep. 9, 153–165. https://doi.org/10.1016/j.celrep.2014.08.066
- Schindelin, J., Arganda-Carreras, I., Frise, E., Kaynig, V., Longair, M., Pietzsch, T., Preibisch, S., Rueden, C., Saalfeld, S., Schmid, B., et al. (2012). Fiji: An open-source platform for biological-image analysis. Nat. Methods 9, 676–682. https://doi.org/10.1038/nmeth.2019.
- Bankhead, P., Loughrey, M.B., Fernández, J.A., Dombrowski, Y., McArt, D.G., Dunne, P.D., McQuaid, S., Gray, R.T., Murray, L.J., Coleman, H.G., et al. (2017). QuPath: Open source software for digital pathology image analysis. Sci. Rep. 7, 16878. https://doi.org/10.1038/s41598-017-17204-5.

- Šali, A., and Blundell, T.L. (1993). Comparative protein modelling by satisfaction of spatial restraints. J. Mol. Biol. 234, 779–815. https://doi.org/10.1006/imbi.1993.1626.
- Eberhardt, J., Santos-Martins, D., Tillack, A.F., and Forli, S. (2021).
 AutoDock Vina 1.2.0: New Docking Methods, Expanded Force Field, and Python Bindings. J. Chem. Inf. Model. 61, 3891–3898. https://doi.org/10.1021/acs.jcim.1c00203.
- Broggi, A., Cigni, C., Zanoni, I., and Granucci, F. (2016). Preparation of single-cell suspensions for cytofluorimetric analysis from different mouse skin regions. J. Vis. Exp. e52589. https://doi.org/10.3791/52589.
- Bender, B.J., Cisneros, A., Duran, A.M., Finn, J.A., Fu, D., Lokits, A.D., Mueller, B.K., Sangha, A.K., Sauer, M.F., Sevy, A.M., et al. (2016). Protocols for Molecular Modeling with Rosetta3 and RosettaScripts. Biochemistry 55, 4748–4763. https://doi.org/10.1021/acs.biochem. 6b00444.
- 55. Abraham, M.J., Murtola, T., Schulz, R., Páll, S., Smith, J.C., Hess, B., and Lindahl, E. (2015). Gromacs: High performance molecular simulations through multi-level parallelism from laptops to supercomputers. SoftwareX 1–2, 19–25. https://doi.org/10.1016/j.softx.2015.06.001.
- Lindorff-Larsen, K., Piana, S., Palmo, K., Maragakis, P., Klepeis, J.L., Dror, R.O., and Shaw, D.E. (2010). Improved side-chain torsion potentials for the Amber ff99SB protein force field. Proteins 78, 1950–1958. https://doi.org/ 10.1002/prot.22711.
- 57. Mesa-Galloso, H., Delgado-Magnero, K.H., Cabezas, S., López-Castilla, A., Hernández-González, J.E., Pedrera, L., Alvarez, C., Peter Tieleman, D., García-Sáez, A.J., Lanio, M.E., et al. (2017). Disrupting a key hydrophobic pair in the oligomerization interface of the actinoporins impairs their pore-forming activity. Protein Sci. 26, 550–565. https://doi.org/10.1002/pro.3104.
- Valdés-Tresanco, M.S., Valdés-Tresanco, M.E., Valiente, P.A., and Moreno, E. (2021). Gmx_MMPBSA: A New Tool to Perform End-State Free Energy Calculations with GROMACS. J. Chem. Theor. Comput. 17, 6281–6291. https://doi.org/10.1021/acs.jctc.1c00645.
- Trott, O., and Olson, A.J. (2010). AutoDock Vina: Improving the speed and accuracy of docking with a new scoring function, efficient optimization, and multithreading. J. Comput. Chem. 31, 455–461. https://doi.org/10. 1002/jcc.21334.
- Baell, J.B., and Holloway, G.A. (2010). New substructure filters for removal of pan assay interference compounds (PAINS) from screening libraries and for their exclusion in bioassays. J. Med. Chem. 53, 2719–2740. https://doi. org/10.1021/jm901137j.





STAR***METHODS**

KEY RESOURCES TABLE

REAGENT or RESOURCE	SOURCE	IDENTIFIER
Antibodies		
Rat anti-mouse MLKL clone 3H1	EMD Millipore Corp	Cat#MABC604; RRID: AB_2820284
Recombinant monoclonal rabbit anti-human MLKL (2B9)	Thermo Fisher Scientific	Cat#MA5-24846; RRID: AB_2717284
Monoclonal mouse anti-α-tubulin	Sigma-Aldrich	Cat#T6199; RRID: AB_477583
Recombinant monoclonal rabbit anti-mouse MLKL ohosphoS345 (EPR9515(2))	Abcam	Cat#ab196436: RRID: AB_2687465
Recombinant monoclonal rabbit anti-human MLKL ohosphoS358 (EPR9514)	Abcam	Cat#ab187091; RRID: AB_2619685
Monoclonal rabbit anti-RIP (D94C12) XP	Cell Signaling Technology	Cat#3493; RRID: AB_2305314
Monoclonal rabbit anti-mouse RIP3 (D4G2A)	Cell Signaling Technology	Cat#95702; RRID: AB_2721823
Rabbit anti-mouse phosphor-RIP (Ser166)	Cell Signaling Technology	Cat#31122; RRID: AB_2799000
Monoclonal rabbit anti-mouse phospho-RIP3 Thr231/Ser232) (E7S1R)	Cell Signaling Technology	Cat#91702; RRID: AB_2937060
Monoclonal mouse anti- GAPDH (D4C6R)	Cell Signaling Technology	Cat#97166; RRID: AB_2756824
Rabbit anti-ubiquitin	Sigma-Aldrich	Cat#07-375; RRID: AB_310565
Rabbit anti- ATP1A1	Proteintech	Cat#14418-1-AP; RRID: AB_2227873
Rabbit anti- VDAC1/2/3	Proteintech	Cat#11663-1-AP; RRID: AB_2304144
Peroxidase AffiniPure™ Goat Anti-Rabbit IgG (H+L)	Jackson Immunoresearch Laboratories	Cat#111-035-003; RRID: AB_2313567
Peroxidase AffiniPure™ Goat Anti-Mouse IgG (H+L)	Jackson Immunoresearch Laboratories	Cat#115-035-003; RRID: AB_10015289
Anti-rat IgG, HRP-linked Antibody	Cell Signaling Technology	Cat#7077; RRID: AB_10694715
Anti-Mouse CD16/CD32 (clone 93)	BD Biosciences	Cat#567021; RRID: AB_2870011
Anti-Mouse CD45-BV711 (clone 30-F11)	BD Biosciences	Cat#563709; RRID: AB_2687455
Anti-mouse/human CD4-AF488 (clone IM7)	Biolegend	Cat#103015; RRID: AB_493678
Anti-Mouse Lys6G-PE (clone 1A8)	Biolegend	Cat#127607; RRID: AB_1186104
RIPK3 Antibody B-2 AC	Santa Cruz Biotechnology	Cat#sc-374639 AC; RRID:AB_1099223
Chemicals, peptides, and recombinant proteins		
Recombinant Human TNF-α	Peprotech	Cat#300-01A
Recombinant Murine TNF-α	Peprotech	Cat#315-01A
Recombinant Human IFN-β	Peprotech	Cat#300-02BC
Smac mimetic LCL-161	Med Chem Express	Cat#HY-15518
Z-VAD-FMK	APEXBIO	Cat#A1902
PS-EB Ultrapure	Invivogen	Cat#tlrl-3pelps
Poly_I:C (HMW)	Invivogen	Cat#tlrl-pic
Poly A:T	Invivogen	Cat#tlrl-patn
Recombinant Mouse IFN-γ	Biolegend	Cat#575302
Recombinant Human IFN-γ	Peprotech	Cat#300-02
Recombinant mouse macrophage colony- stimulating factor (M-CSF)	Immunotools	Cat#13343113
Doxycycline hyclate (DOX)	Med Chem Express	Cat# HY-N0565B
PR-619	Med Chem Express	Cat#HY-13814
MG132 CAS 133407-82-6 – Calbiochem	Millipore	Cat#474790
Recombinant Human GST-USP21 Catalytic Domain Protein	R&D Systems	Cat#E-622

Article



Continued		
REAGENT or RESOURCE	SOURCE	IDENTIFIER
Propidium Iodide (PI)	Sigma-Aldrich	Cat#25535-16-4
DRAQ7™ Dye	Invitrogen	Cat# D15106
Puromycin dihydrochloride from Streptomyces alboniger	Sigma-Aldrich	Cat#P8833
L-α-phosphatidylcholine (Egg, Chicken) (PC)	Avanti Polar Lipids	Cat#840051
L-α-phosphatidylethanolamine (Egg, Chicken) (PE)	Avanti Polar Lipids	Cat#840021
L-α-phosphatidic acid (Egg, Chicken) (PA)	Avanti Polar Lipids	Cat#840101
L-α-phosphatidylserine (Brain, Porcine) (PS)	Avanti Polar Lipids	Cat#840032
L- α -phosphatidylinositol-4,5-bisphosphate (Brain, Porcine) (PI(4,5)P $_2$)	Avanti Polar Lipids	Cat#840046
(MBA-h1) N-{3-[6-(4-methylpiperazin-1-yl)pyridazin-3-yl]phenyl}naphthalene-2-carboxamide	MolPort	Cat#Molport-003-157-351
(MBA-m1) N-(3-chloro-4-naphthalen-2-yloxyphenyl)- 6-methoxy-2-methylquinolin-4-amine	MolPort	Cat#MolPort-002-540-214
GENEzoI TM	Geneaid Biotech	Cat#GZR050
TRIzol™	Thermo Fisher Scientific	Cat#15596018
Lipofectamine™ 2000 Transfection Reagent	Invitrogen	Cat#11668027
BLOXALL® Endogenous Blocking Solution, Peroxidase and Alkaline Phosphatase	Vector Laboratories	Cat#SP-6000-100
Sequencing Grade Modified Trypsin	Promega	Cat#V5111
Polybrene Infection/Transfection Reagent	Sigma-Aldrich	Cat#TR-1003
SuperSignal™ West Pico PLUS Chemiluminescent Substrate	Thermo Scientific	Cat#34580
Critical commercial assays		
Q5® Site-Directed Mutagenesis Kit	New England Biolabs	Cat#E0554S
NucleoSpin RNA/Protein	Macherey-Nagel	Cat#740933.50
Luna® Universal One-Step RT-qPCR Kit	New England Biolabs	Cat#E3005L
PowerUp™ SYBR™ Green	Applied Biosystems	Cat#A25742
GFP-Trap® Magnetic Agarose beads	ChromoTek	Cat#gtma
Mouse IL-1 beta Uncoated ELISA Kit with Plates	Invitrogen	Cat#88-7013-22
Mouse MIP-1a (CCL3) Uncoated ELISA Kit with Plates	Invitrogen	Cat#88-56013-22
Mouse IL-6 Uncoated ELISA Kit with Plates	Invitrogen	Cat#88-7064-22
ImmPRESS®-AP Goat Anti-Rat IgG (Mouse Adsorbed) Polymer Detection Kit, Alkaline Phosphatase	Vector Laboratories	Cat#MP-5444-15
ImmPACT® Vector® Red Substrate Kit, Alkaline Phosphatase (AP)	Vector Laboratories	Cat#SK-5105
Gateway™ LR Clonase™ II Enzyme mix	Thermo Fisher Scientific	Cat#11791020
Glutathione Sepharose™ 4B	Cytiva	Cat#17075601
anti-Flag® M2 Magnetic beads	Milipore	Cat#M8823
Trichrome Stain (Masson) Kit	Sigma-Aldrich	Cat#HT15
Deposited data		
Unprocessed blots and imaging data	This paper	Mendeley data: https://doi.org/10.17632/ c56wwg84sp.1
Experimental models: Cell lines		
MDFs: Mlkl ^{WT/WT}	Dr. Lynn Wong	N/A
MDFs: MIKI ^{-/-}	Dr. Lynn Wong	N/A
MDFs: Mlkl ^{m1/m1} , Mlkl ^{m2/m2}	This paper	N/A
MDFs: mMLKL1-GFP, mMLKL2-GFP, mMLKL2- GFP_mMLKL1-Flag, mMLKL1-GFP_mMLKL2-Flag	This paper	N/A
NIH: Mikl ^{WT/WT}	Dr. Stefan Krautwald	N/A
		(Continued on next page



Continued		
REAGENT or RESOURCE	SOURCE	IDENTIFIER
NIH-3T3: CRISPR/Cas9 <i>Mlkl^{-/-}</i>	Moerke et al.45	N/A
HT-29: <i>Miki^{WT/WT}</i>	Dr. Klaus Schulze- Osthoff	N/A
HT-29: CRISPR/Cas9 Mlkl ^{-/-}	Gong et al.46	N/A
HT-29: sh_hMLKL0	This paper	N/A
HT-29: hMLKL0-GFP, hMLKL1-GFP, hMLKL1- GFP_hMLKL0-Flag	This paper	N/A
HEK-293T: <i>MIkl^{WT/WT}</i>	Dr. Frank Essmann	N/A
A549: Mlkl ^{WT/WT}	Dr. Henning Walzack	N/A
HeLa-hRIPK3	Lafont et al.47	N/A
L929: <i>Mlkl^{WT/WT}</i>	Dr. Douglas Green	N/A
L929: CRISPR/Cas9 Mlkl ^{-/-}	Gong et al.46	N/A
Experimental models: Organisms/strains		
C57BL/6N: MIKI ^{m1/m1} , MIKI ^{m2/m2}	This paper	N/A
C57BL/6N: MIkI ^{m1/m1} ;Ripk ^{E-KO} , MIkI ^{m2/m2} ;Ripk ^{E-KO}	This paper	N/A
C57BL/6N: MIkI ^{WT/WT1} ;Ripk ^{E-KO}	Dannappel et al. ²⁸	N/A
C57BL/6N: <i>Tnfr^{-/-};Hoip^{E-KO}</i>	Peltzer et al. ⁴⁸	N/A
Oligonucleotides		
shRNA targeting hMLKL0: 5'-TGGTAGGGTTCTTTCTGAAAT-3'	This paper	N/A
crRNA targeting 5'splice donor site in exon 10 of mouse Mlkl: 5'- AGACTCCTACCGTCCACAGA-3'	This paper	N/A
ssODN for generation of <i>Mlkl</i> ^{m1/m1} : 5'-TGAGTTGTTGCGGGAAA TCATTAATGAGTGTCGTGCCCATGAGCCCTCCCAACGGCCCT CgGTGGACGGAAGGAGTCTTTCTGGCAGAGAACGTAAGCCG CGTGTTGATTTCACGATTGTGAAAGGTTTC-3'	This paper	N/A
crRNA targeting 3'splice donor site in exon 10 of mouse <i>Mlkl</i> : 5'-ACAATCGTGAAATCAACACG-3'	This paper	N/A
ssODN for generation of MIkI ^{m2/m2} : 5'-GTGCCCATGAGCCCTC CCAACGGCCCTCTGTGGACGGTAGGAGTCTTTCTGGCAGAG AACcTAAGCtGCGTGTTGATTTCACGATTGTGAAAGGTTTCTT TTGTTTGATTTTTGGTTTCGGCTTTGG-3'	This paper	N/A
Recombinant DNA		
Plasmid: Gateway™ pENTR™ 11 Dual Selection Vector	Invitrogen	Cat#A10467
Plasmid: plnducer20	Addgene	Cat#44012
Plasmid: pLenti CMV Puro DEST (w118-1)	Addgene	Cat#17452
Plasmid: PMD2.G	Addgene	Cat#12259
Plasmid: PSPAX2	Addgene	Cat#12260
Plasmid: EZ-Tet-pLKO-Puro vector	Addgene	Cat#85966
Plasmid: pEGFP-N2	Dr. Frank Essmann	N/A
Plasmid: pEGFP-N2_mMLKL2_8Ala and	This paper	N/A
Plasmid: pEGFP-N2_mMLKL2_6Ala	This paper	N/A
Plasmid: pEGFP-N2_mMLKL2_4Ala	This paper	N/A
Plasmid: pEGFP-N2_mMLKL2_2Ala	This paper	N/A
Plasmid: pEGFP-N2_hMLKL1_8aa	This paper	N/A
Plasmid: pEGFP-N2_hMLKL0	This paper	N/A
	This paper	N/A
Plasmid: pEGFP-N2_hMLKL2_8aa	This paper	
Plasmid: pEGFP-N2_hMLKL2_8aa Plasmid: pEGFP-N2_mMLKL2_∆448-464	This paper This paper	N/A
·		N/A N/A
Plasmid: pEGFP-N2_mMLKL2_Δ448-464	This paper	

Article



Continued			
EAGENT or RESOURCE	SOURCE	IDENTIFIER	
lasmid: pEGFP-N2_mMLKL2_L450R_S454R	This paper	N/A	
lasmid: pEGFP-N2_mMLKL2_I84A_F87A	This paper	N/A	
asmid: pEGFP-N2_hMLKL1_C86D	This paper	N/A	
lasmid: pEGFP-N2_hMLKL1_C86D_S467D	This paper	N/A	
asmid: pEGFP-N2_mMLKL1_S345D_S347D	This paper	N/A	
lasmid: pEGFP-N2_mMLKL2_S345D_S347D	This paper	N/A	
lasmid: pEGFP-N2_hMLKL0_T357E_S358D	This paper	N/A	
asmid: pEGFP-N2_hMLKL1_T357E_S358D	This paper	N/A	
asmid: pEGFP-N2_hMLKL0_T357E_S358D	This paper	N/A	
asmid: pEGFP-N2_hMLKL1_K230M	This paper	N/A	
lasmid: pEGFP-N2_mMLKL_4HB (1-125)	This paper	N/A	
asmid: pEGFP-N2_mMLKL_4HB+brace (1-165)	This paper	N/A	
asmid: pEGFP-N2_mMLKL2_S345D_S347D_Δ448-464	This paper	N/A	
asmid: pEGFP-N2_mMLKL2_S345D_S347D_L450R_S454R	This paper	N/A	
asmid: pEGFP-N2_hMLKL1_T357E_S358D_8aa	This paper	N/A	
lasmid: pEGFP-N2_hMLKL1_T357E_S358D_Δ462-471	This paper	N/A	
asmid: pEGFP-N2_hMLKL1_T357E_S358D_C86D	This paper	N/A	
lasmid: pEGFP-N2_hMLKL1_T357E_S358D_C86D_S467D	This paper	N/A	
lasmid: pEGFP-N2_hMLKL1_K230M_8aa	This paper	N/A	
lasmid: pEGFP-N2_hMLKL1_K230M_Δ462-471	This paper	N/A	
asmid: pEGFP-N2_hMLKL1_K230M_C86D	This paper	N/A	
lasmid: pEGFP-N2_hMLKL1_K230M_C86D_S467D	This paper	N/A	
lasmid: pEGFP-N2_mMLKL1_E161A_I162A	This paper	N/A	
lasmid: pEGFP-N2_mMLKL1_N163A_K164A	This paper	N/A	
lasmid: pEGFP-N2_mMLKL2_S89C_L450C	This paper	N/A	
lasmid: pEGFP-N2_mMLKL2_I151C_S454C	This paper	N/A	
lasmid: pEGFP-N2_mMLKL2_Y307C_L450C	This paper	N/A	
lasmid: pEGFP-N2_mMLKL2_L427C_L453C	This paper	N/A	
lasmid: pEGFP-N2_hMLKL1_N155C_F469C	This paper	N/A	
lasmid: pEGFP-N2_hMLKL1_V310C_L466C	This paper	N/A	
·		N/A	
lasmid: pEGFP-N2_hMLKL1_L311C_L466C	This paper	N/A	
lasmid: pEGFP-N2_hMLKL1_L441C_L466C	This paper		
lasmid: pEGFP-N2_hRIPK3 (no tag)	This paper	N/A	
lasmid: pENTR™_mMLKL1-GFP	This paper	N/A	
lasmid: pENTR™_mMLKL2-GFP	This paper	N/A	
lasmid: pENTR™_mMLKL1-Flag	This paper	N/A	
lasmid: pENTR™_mMLKL2-Flag	This paper	N/A	
lasmid: pENTR™_hMLKL0-GFP	This paper	N/A	
lasmid: pENTR™_hMLKL1-GFP	This paper	N/A	
lasmid: pENTR™_hMLKL0-Flag	This paper	N/A	
asmid: pLenti _mMLKL1-Flag	This paper	N/A	
asmid: pLenti mMLKL2-Flag	This paper	N/A	
asmid: pLenti hMLKL0-Flag	This paper	N/A	
asmid_ plnducer20_mMLKL1-GFP	This paper	N/A	
asmid_ pInducer20_mMLKL2-GFP	This paper	N/A	
lasmid_ pInducer20_hMLKL0-GFP	This paper	N/A	
lasmid_ plnducer20_hMLKL1-GFP	This paper	N/A	
oftware and algorithms	·		



Continued			
REAGENT or RESOURCE	SOURCE	IDENTIFIER	
FACSDiva	BD Biosciences	https://www.bdbiosciences.com/en-us/ products/software/instrument-software/ bd-facsdiva-software	
IncuCyte bioimaging platform	Sartorius	Version 2020B	
Perseus	MaxQuant	Version 1.6.15.0	
MaxQuant	MaxQuant	Version 1.5.3.8	
Originpro 2018	Origin Lab	https://www.originlab.com/2018	
NanoTemper	Nano Temper Tech	https://nanotempertech.com/	
PEAQ	Marvel Analytical	https://www.malvernpanalytical.com/en/ products/product-range/microcal-range/ microcal-itc-range/microcal-peaq-itc	
FlowJo	BD Biosciences	https://www.flowjo.com/solutions/flowjo/downloads	
LAS X Life Science Microscope Software	Leica Microsystems	https://www.leica-microsystems.com/ products/microscope-software/p/leica- las-x-ls/downloads/	
QuPath	Bankhead et al. ⁵⁰	https://qupath.github.io/	
Vevo 3100	Visualsonics	https://www.visualsonics.com/product/imaging-systems/vevo-3100	
MODELLER	Šali and Blundell ⁵¹	Version 9.14	
GROMACS	gromacs.org	Version 5.1.4	
Autodock Vina	Eberhardt et al. ⁵²	https://vina.scripps.edu/	
GraphPad Prism	GraphPad	Version 10.1.1	

EXPERIMENTAL MODEL AND STUDY PARTICIPANT DETAILS

Primary cells and cell lines

For the characterization of mouse MLKL isoforms, we primarily used $Mlkl^{-/-}$ NIH-3T3, $Mlkl^{-/-}$ L929, and $Mlkl^{-/-}$ MDF cell lines, as these cells are common models to study necroptosis. In transient experiments with mutants, $Mlkl^{-/-}$ NIH-3T3 cells were the choice as they are easier to transfect. $Mlkl^{-/-}$ MDF cell lines were used for stable cell line generation as it is the wildest used cellular system for necroptosis. Primary cells were isolated from mice expressing either one or the two isoforms in order to evaluate their role under endogenous and more physiological conditions. For the characterization of human MLKL isoforms and mutants, HEK cells were primarily used in transient transfection experiments, as they are easy to transfect. Based on results obtained with transient transfection systems, we then came back to HT-29 cells and generated stable systems or knockdown for hMLKL0.

All cells were cultured in low glucose Dulbecco's Modified Eagle Medium (DMEM, Sigma-Aldrich, Germany) supplemented with 10% Fetal Bovine Serum (FBS) and 1% penicillin-streptomycin (ThermoFisher, Germany), and grown in a humidified incubator containing 5% CO $_2$ at 37° C. The cells were frequently passaged at sub-confluence and seeded at a density of $1-5 \times 10^4$ cells/mL. Primary lung fibroblasts were isolated from the lungs of 6-12-week-old mice and cultured in low glucose DMEM supplemented with 10% FBS and penicillin-streptomycin. Primary BMDMs were obtained from the bone marrow of 6-12-week-old mice and further cultivated with media supplemented with 50×10^4 mouse macrophage colony-stimulating factor (M-CSF) (ImmunoTools, Germany) and cultured in low glucose DMEM 10% FBS and penicillin-streptomycin.

Stable cell line generation

MLKL isoforms were cloned into GatewayTM pENTRTM 11 Dual Selection Vector either tagged with Flag (GATTATAAAG ATGATGATAAA) or fused to the GFP sequence. The sequences or the primers used are summarized in table S1. The sequences were then introduced into both pLenti CMV Puro DEST (w118-1) and plnducer20 vectors using GatewayTM LR ClonaseTM II Enzyme mix from Invitrogen (Germany). For inducible short hairpin RNA (shRNA) generation, the sequence TGGTAGGGTTCTTTCTGAAAT, which specifically targets hMLKL0, was introduced in the EZ-Tet-pLKO-Puro vector. For lentivirus production, HEK-293T cells were co-transfected with the lentiviral vectors and the packaging vectors PMD2.G and PSPAX2. The viruses were harvested by centrifugation for 5 min at 500 g and target cells ($Mlkl^{-/-}$ MDF or $MLKL^{-/-}$ HT-29 cells) were then infected with the virus using Polybrene Infection/Transfection Reagent from Sigma-Aldrich (Germany). Inducible cell lines expressing MLKL-GFP were treated with 1.0 μ g/mL DOX for 12 h and selected for GFP signal by fluorescence-activated cell sorting (FACS). Cells expressing MLKL-flag were selected by treatment with 5.5 μ g/mL puromycin for 48 h.

Article



Animal breeding and organ isolation

C57BL/6 mice were bred in OHB-level rooms (LASC UZH) and organs were snap-frozen in liquid nitrogen following isolation under the animal license 186/2015. *Tnfr1*^{-/-};*Hoip*^{E-KO} C57BL/6 mice were bred in a specific-pathogen-free (SPF) level room (BSU-UCL) and housed in IVC cages.

Mouse generation

For Mlk/m1/m1 mice (lacking mMLKL2), a CRISPR/Cas9 ribonucleoprotein (RNP) complex consisting of a specific crRNA (5'-AGACTCCTACCGTCCACAGA-3') targeting close to the 5' splice donor site in exon 10 of the Mlkl gene, tracrRNA (IDT) and the Cas9 protein (IDT) was co-injected into fertilized WT oocytes together with a long single-stranded oligodeoxynucleotide (ssODN) (5'-TGAGTTGTTGCGGGAAATCATTAATGAGTGTCGTGCCCATGAGCCCTCCCAACGGCCCTCgGTGGACGGaAGGAGTCTTTCTG GCAGAGAACGTAAGCCGCGTGTTGATTTCACGATTGTGAAAGGTTTC-3') containing the desired mutations (indicated in lowercase letters). Mutating this splice donor should prevent the formation of mMLKL2. For Mlklm2/m2 mice (lacking mMLKL1) the strategy was similar, with the specific crRNA (5'-ACAATCGTGAAATCAACACG-3') targeting close to the 3' splice donor site of the same exon and using a different long ssODN (5'-GTGCCCATGAGCCCTCCCAACGGCCCTCTGTGGACGGTAGGAGTCTTTCTGGCAGAGAACC the formation of mMLKL1. After confirmation of the correct mutations by genomic DNA sequencing analysis, founder mice carrying the targeted mutations were backcrossed to C57BL/6N mice to establish independent mouse lines. Mlkl^{m1/m1};Ripk^{E-KO} and $Mlkl^{m2/m2}$; $Ripkl^{E-KO}$ mice where generated by crossing $Mlkl^{m1/m}$ and $Mlkl^{m2/m2}$ mice into the $Ripkl^{E-KO}$ mouse line (i.e. RIPK1FL mice with a K14Cre allele). 3,28 Mice were maintained at the SPF animal facilities of the CECAD Research Center of the University of Cologne. All mouse procedures were conducted in accordance with national and institutional guidelines, and protocols were approved by the responsible local authorities in Germany (Landesamt für Natur, Umwelt und Verbraucherschutz Nordrhein-Westfalen).

Mouse model of MLKL-dependent dermatitis

 $Tnfr1^{-/-}$; $Hoil-1^{E-KO}$ mice were treated with 30 mg/kg of MBA-m1 or with the vehicle when lesions were evident (between 30 and 40 days of age). Briefly, 30 μ g/ μ l MBA-m1 (in DMSO) was diluted 1/10 in PEG4000 (Qiagen, Germany) and injected i.p. every-other day for three weeks. All mice were genotyped by PCR analysis and were fed *ad libitum*. All animal experiments were conducted under an appropriate UK project license in accordance with the regulations of UK home office for animal welfare according to ASPA (animal (scientific procedure) Act 1986).

Mouse model of MLKL-dependent abdominal aortic aneurysm

WT mice were injected with pacreatic porcine elastase (PPE) to induce aneurysm development. Specifically, the PPE infusion was performed in 10 to 14-week-old males. Animals were treated over 18 days every other day, either with vehicle or MBA-m1, starting 4 days prior to PPE injection. Samples were collected and analyzed 28 days after PPE treatment. In brief, after placing temporary ligatures around the proximal and distal aorta, the infrarenal aorta was infused with elastase from porcine pancreas for 5 min at 100 mmHg. Body temperature was kept constant at 37°C by a heating pad. After removing the infusion catheter, the aortotomy was sutured and the abdomen was closed. The abdominal segments were harvested at 3 or 28 days post-PPE surgery. For histological and immunofluorescence staining, the aorta was perfused with saline followed by 1.5% agarose before harvesting. To obtain ultrasound images of the abdominal aorta, the mice were anesthetized with continuously delivered 2% isoflurane gas inhalation. Ultrasound gel was applied to the depilated skin of the abdomen and imaging was performed with a Vevo3100 imaging system (VisualSonics). B-mode, M-mode and EKV recordings were performed using a MX550D linear array transducer (25-55 MHz, Centre Transmit: 40 MHz, Axial Resolution: 40 μm) with a frame rate of 230-400 frames/s. All ultrasound images were analyzed using the Vevo 3100-software and parameters like aortic diameter, pulse wave velocity (PWV) and aortic wall thickness were calculated. Masson Trichrome staining was performed using Trichrome Stain (Masson) Kit (HT15, Sigma) according to the manufacturer's protocol. Images were acquired with a BZ-X800 microscope system (Keyence, IL, USA). For elastin fibers, the tissue sections were imaged for the elastin autofluorescence using the GFP filter on BZ-X800 microscope system (Keyence, IL, USA). All images were analysed using ImageJ software.

METHOD DETAILS

Generation of mouse and human MLKL mutants

mMLKL2 was generated by deleting the sequence corresponding to the eight amino acid insertion in mMLKL1. The following alterations in mouse and human MLKLisoforms were carried out: (1) insertion at position 448 of mMLKL2 of either 2, 4, 6, or 8 Ala residues, insertion at position 461 of hMLKL1 of the RSLSGRER sequence (from mMLKL1) namely hMLKL1_8aa, or the extra five amino acids sequence GRVLS to generate hMLKL0, insertion at position 253 of hMLKL2 of the RSLSGRER sequence namely hMLKL2_8aa; (2) C-terminal deletions namely mMLKL2_ Δ 448-464, mMLKL2_ Δ 457-464, hMLKL1_ Δ 462-471, and hMLKL2_ Δ 254-263; (3) hydrophobic groove mutants namely mMLKL2_L450R_S454R, mMLKL2_I84A_F87A, hMLKL1_C86D, and hMLKL1_C86D_S467D; (4) the phosphomimetic mutants mMLKL1_S345D_S347D, mMLKL2_S345D_S347D, hMLKL0_T357E_S358D, and hMLKL1_T357E_S358D; (5) the intrinsically



active mutants hMLKL1_K230M, mMLKL_4HB (1-125), and mMLKL_4HB+brace (1-165); (6) the combined mutants mMLKL2_S345D_S347D_Δ448-464, mMLKL2_S345D_S347D_L450R_S454R, hMLKL1_T357E_S358D_8aa, hMLKL1_T357E_S358D_Δ462-471, hMLKL1_T357E_S358D_C86D, hMLKL1_T357E_S358D_C86D_S467D; hMLKL1_K230M_8aa, hMLKL1_K230M_Δ462-471, hMLKL1_K230M_C86D and hMLKL1_K230M_C86D_S467D; (7) Ala mutations in the Br region of mMLKL1 namely mMLKL1_E161A_I162A and mMLKL1_N163A_K164A; (8) Cys mutations in the Hc, 4HB, Br or psK region of mMLKL2 namely mMLKL2_S89C_L450C, mMLKL2_I151C_S454C, mMLKL2_Y307C_L450C, and mMLKL2_L427C_L453C or hMLKL namely hMLKL1_N155C_F469C, hMLKL1_V310C_L466C, hMLKL1_L311C_L466C, and hMLKL1_L441C_L466C. All insertions, deletions, and mutations were carried out using the Q5® Site-Directed Mutagenesis Kit (New England Biolabs, Inc., MA, USA) and sequenced-confirmed (Eurofins Genomics Germany GmbH, Germany). The sequence of all primers used is listed in Table S1.

Transient transfection

The day after seeding, cells were transfected with Lipofectamine 2000 (Invitrogen, Germany), between 200-800 ng of the corresponding DNA in Opti-MEM (Thermofisher, Germany) and DMEM supplemented with FBS and antibiotics, for 24 h.

Treatments to induce expression of MLKL

For quantitative reverse transcription polymerase chain reaction (RT-qPCR) experiments, mouse cells were seeded in a 6-well plate to achieve 50-70% confluency and treated the next day with 100 ng/mL LPS, 30 ng/mL IFN γ or 30 ng/mL mouse TNF for 6 h. Human cell lines were treated with human IFN γ or 30 ng/mL human IFN β , 30 ng/mL human TNF for 6 h. For WB analysis, lung fibroblasts or BMDMs were seeded in a 10-cm dish to achieve 50-70% confluency and treated either with 200 nM MG132 (0-48 h), 100 ng/mL LPS (1, 2, 4, or 8 h), mouse 30 ng/mL TNF or 30 ng/mL IFN γ (8 h).

RNA isolation and RT-qPCR

For the extraction and quantification of RNA in mouse tissues, isolation of RNA was carried out using GENEzol (Geneaid Biotech Ltd., Taiwan) or TRIzol (ThermoFisher, Switzerland) following the manufacturer's protocol. The isolated RNA, 1 μ g from mouse organs or 200 ng from cells, was then transcribed with a Multiscribe Transcriptase (ThermoFisher, Switzerland) following the manufacturer's instructions. For the analysis of the expression upon stimulation, RNA extraction was performed using the NucleoSpin RNA, Mini kit for RNA purification (Macherey-Nagel, Germany). Then, qPCR assay was performed using the Luna® Universal One-Step RT-qPCR Kit (New England Biolabs, Inc., MA, USA). Powerup Sybr Green (ThermoFisher, Switzerland) The sequences of the used primers are summarized in Table S2.

Treatments for necroptosis induction

Cells were treated with any of the following: (1) a mixture of the mouse or human TNF (T) (30 ng/mL), smac mimetic LCL-161 (S) (20 μ M), and the pan-caspase inhibitor zVAD (Z) (20 μ M), (2) The dsRNA analog Poly_I:C (100 μ g/mL) and zVAD (20 μ M) to activate the TLR3 pathway, (3) LPS (1 μ g/mL) and zVAD (20 μ M) to activate the TLR4 pathway, and (4) the dsDNA analog Poly_A:T and zVAD (20 μ M) to activate the ZBP1 pathway. BMDMs were first preincubated with zVAD for 6 h and then treated with LPS. In hMLKL0 knockdown experiment, HT-29 cells were treated with human TNF (T) (10 ng/mL), smac mimetic LCL-161 (S) (5 μ M), and the pancaspase inhibitor zVAD (Z) (20 μ M).

Flow cytometry assays

Flow cytometric analyses were performed on a Beckman Coulter CytoFlex S using the FACSDiva software (Krefeld, Germany). Briefly, cells were seeded, transfected, and treated as described above. The day after necroptosis induction or overexpression, the detached population was collected and pooled together with the remained cells, that were detached with trypsin. The pelleted cells were washed twice with Phosphate-Buffered Saline (PBS, Sigma-Aldrich, Germany) and centrifuged for 5 min at 500 g and 4 $^{\circ}$ C. The cells were then resuspended in 150 μ L of PBS, incubated with PI (2 μ g/mL) for 15 min at room temperature, and analyzed. A total of 10 000 cells were counted and disrupted membrane integrity was determined with PI-positive staining. In transfected cells, the dead cell population was calculated from the PI-positive cells within the GFP-positive population.

Incucyte experiments

Kinetics of cell death were followed using the IncuCyte bioimaging platform (Essen, UK). In this case, cells were seeded in 96-well plates (10^4 cells per well) one day before treatment. After treatment, four images per well were captured, analyzed, and averaged. Cell death was measured by the incorporation of 0.1 μ M DRAQ7. Data was collected as a count of DRAQ7 positive cells and normalized taking as 100% the maximum count of cell death in the experiment or the transfected population or using cell-by-cell analysis.

Brightfield and confocal microscopy

Cells were seeded in DMEM in 8-well Ibidi chambers (Ibidi, Germany), transfected, and induced to undergo necroptosis as described above. Cells were also loaded with PI (2 μ g/mL) simultaneously with TSZ treatment. Images were recorded using a Zeiss LSM 710 ConfoCor3 microscope (Carl Zeiss, Germany) equipped with a humidified incubator maintained at 5% CO₂ and 37°C, using a Zeiss

Article



C-Apochromat 40X, NA=1.2 water immersion objective. Fluorophore excitation was achieved with argon (488 nm) and HeNe (561 nm) lasers. Shown pictures are representative of at least three independent experiments.

TIRF

Cells were seeded in DMEM in 8-well Ibidi chambers (Ibidi, Germany), transfected, and induced to undergo necroptosis as described above. The cells were then treated with $0.5 \,\mu\text{g}/\mu\text{L}$ DOX for 1 h. The media was then replaced with TSZ and single MLKL-GFP particles at the plasma membrane were imaged with a TIRF microscope. For the density analysis, single particles of MLKL-GFP were quantitatively analyzed with TrackMate, while the cell boundaries were manually traced and measured in Fiji ImageJ.

Western blotting

After treatment, the detached cell population was collected and pooled with the harvested attached cells, washed with PBS, and lysed with RIPA buffer (Thermofisher, Germany) supplemented with phosphatase inhibitors (Roche, Germany) and protease inhibitors (Roche, Germany). In the case of experiments with primary cells, lysis buffer (10 mM Tris/Cl pH 7.5, 150 mM NaCl,0.5 mM EDTA, 0.5% nonidet NP-40) was used as an alternative to RIPA. The lysis was performed for 20 min on ice, followed by centrifugation for 20 min at 15000 *g* and 4°C. Afterwards, the supernatants were collected, quantified, and mixed with SDS sample buffer with β-mercaptoethanol (BME). Samples were then heated at 95°C for 10 min and resolved using either reducing or non-reducing SDS-PAGE (12% or 4 to 15% gradient) gels, transferred onto a nitrocellulose membrane (Bio-Rad, Germany), and probed with antibodies specific to human and mouse MLKL, or the phosphorylated human and mouse MLKL. Bands were visualized in a dark room, with a developer machine and using the SuperSignalTM West Pico PLUS Chemiluminescent Substrate (ThermoScientific, Germany). Shown blots are representative of at least two independent experiments.

Subcellular fractionation

After treatment, cells were resuspended in isolation buffer (250 mM sucrose, 5 mM Tris, 2 mM EDTA, pH 7.4), and then mechanically lysed using a 25G 0.5×25 mm syringe, passing the sample through the syringe 40 times. The cell lysate was then centrifuged for 10 min at 14 000 g, and the supernatant was further centrifuged for 1 h at 100 000 g and 4°C. From this last centrifugation the supernatant was collected as a cytosolic fraction, and the pellet was washed, centrifuged 1 h at 100 000 g and 4°C and finally collected as the membrane fraction. Both, cytosolic and membrane fractions were mixed with SDS-PAGE sample buffer with or without reducing agents, heated, and loaded into a 12% or a 4 to 15% gradient gel. Protein separation, transfer, and detection were carried out as described before.

TUBE affinity precipitation

After treating the cells with the indicated stimuli, cells were harvested using a scraper. The cell pellet was then lysed in lysis buffer (1% triton, 10% glycerol, 30 mM TRIS-HCl, 150 mM NaCl, 20 μ M PR-619, pH 7.4) with PR-169 and phosphatase and protease inhibitors. The supernatant recovered after centrifugation was further processed for the TUBE pull-down. 50 μ g/mL of GST-TUBE (produced inhouse) was added to the lysates and incubated at 4°C. After 2 h of incubation, 30 μ L Glutathione SepharoseTM 4B (GE Healthcare, Sweden) beads were added to each lysate and further incubated overnight at 4°C. Samples were washed four times with washing buffer (1% triton, 5% glycerol, 30 mM TRIS-HCl, 150 mM NaCl, pH 7.4) and then sample elution from beads was performed by adding SDS loading dye to the lysates, followed by boiling. Samples were then loaded into an SDS-PAGE gel and subsequently processed for WB.

Cellular thermal shift assays

NIH-3T3 cells were seeded to obtain 3 x 10^5 cells per temperature point. Cells were treated for 1 h with DMSO or $10~\mu$ M MBA-m1 either in the presence or the absence of TSZ. Cells were pelleted, washed with PBS and resuspended in $100~\mu$ L PBS and loaded into PCR tubes. An additional centrifugation step was done to remove the supernatant. Then, cells were heated at a given temperature for 3 min, and cooled at room temperature for 1 min, using a Thermal Cycler (Bio-Rad, Germany). Cells were resuspended in lysis buffer (20 mM Tris-HCl, 120~mM NaCl, 0.5%~nNP-40, pH 8) with protease inhibitors and subjected to three cycles of freezing and thawing for lysis. The soluble and precipitated fractions of proteins were separated by centrifugation for 30 min at 13~000~g and 4° C. Soluble protein fractions were resolved by SDS-PAGE and analyzed by WB.

Co-immunoprecipitation assays

For the co-immunoprecipitation of endogenous RIPK3 and MLKL, agarose beads with the coupled antibody (RIPK3 Antibody B-2 AC, cat: sc-374639 AC, 25% agarose) were added to each sample and incubated with rotation at 4° C overnight. The next day, the samples were centrifuged at 1000 g to precipitate the beads. The supernatant was collected as the flow-through fraction and the beads were washed three times with PBS following the same procedure. After the last wash, the beads were resuspended in PBS, and samples were prepared for SDS-PAGE using a non-reducing sample buffer. The samples were then loaded and processed using the Jess Automated Western Blot System (ProteinSimple, Bio-Techne, MN, USA).

For the co-immunoprecipitation of mMLKL1 and mMLKL2, Flag-tagged mMLKL1 was purified using anti-Flag® M2 Magnetic beads (Sigma-Aldrich, Germany). The fraction of mMLKL2-GFP that co-immunoprecipitated with mMLKL1 was specifically detected



by WB, using and anti-GFP antibody. For the co-immunoprecipitation of mMLKL variants and RIPK1/3, GFP variants of mMLKL were purified using ChromoTek GFP-Trap® Magnetic Agarose beads (ThermoScientific, Germany). After it, RIPK1/3 were detected by mass spectrometry (MS). Samples were digested on beads following one step of incubation with elution buffer I (50 mM Tris-HCl pH 7.5, 2 M urea, 5 μg/mL Sequencing Grade Modified Trypsin* (Promega, Germany), 1 mM dithiothreitol (DTT), for 30 min, and with constant shaking at 400 rpm, at 30°C. After this time, the supernatant was collected and kept. Two consecutive steps of onbeads digestion were performed by incubation with elution II (50 mM Tris-HCl pH 7.5, 2 M urea, 40 mM chloroacetamide (CAA)). The supernatant resulting from each step was collected together with the one obtained from elution I and incubated ON, with constant shaking at 400 rpm, at 32°C, and protect from light. Finally, 1% of trifluoroacetic acid was added to stop the reaction. The resulting peptides were purified using SDB-RP Stage tips (Sigma-Aldrich, Germany).

Peptide detection was performed using a Q-Exactive Plus mass spectrometer coupled to an EASY nLC 1000 or 1200 UPLC (Thermo Scientific). Samples were loaded onto an in-house packed analytical column (50 cm × 75 μm l.D., filled with 2.7 μm Poroshell EC120 C18 (Agilent, CA, USA) that has been equilibrated in solvent A (0.1% formic acid in water) and peptides were separated at a constant flow rate of 250 nL/min using a 50 min gradient followed by a 10 min wash with 95% Solvent B (0.1% formic acid in 80% acetonitrile [ACN]). MS1 survey scans were acquired from 300 to 1750 m/z at a resolution of 70 000. The top ten most abundant peptides were isolated within a 1.8 Th window and subjected to fragmentation at a normalized collision energy of 27%. Product ions were detected at a resolution of 35 000. Precursors were dynamically excluded for 10 sec. All MS raw data were processed with MaxQuant (version 1.5.3.8) using default parameters. The minimal peptide length was set to seven amino acids and carbamidomethylation at cysteine residues was considered as a fixed modification. LFQ quantification on unique peptides was enabled by default settings. The data set was imported into Perseus (version 1.6.15.0) and missing values were replaced using MinDet (q=0.0001) imputation from the ImputeLCMD R package implemented in Perseus (version 1.6.15.0).

Detection of human isoforms by mass spectrometry

Samples from HT-29 cells were collected and lysed with urea buffer (8 M urea in 500 mM Triethylamonium bicarbonate (TEAB)) in the presence of protease inhibitors and Benzonase® Nuclease (Merck, Germany). The supernatant was collected after sample centrifugation at 20 000 g, for 15 min. Samples were digested following incubation with 5 mM DTT, for 1 h, at 25°C, further incubation with 40 mM CAA for 30 min in the dark, and with lysyl endopeptidase, at an enzyme:substrate ratio of 1:75, for 4 h at 25°C. After, further dilution of the sample with 50 mM TEAB to achieve a final concentration of urea \leq 2M, samples were incubated with trypsin at an enzyme:substrate ratio of 1:75, ON, at 25°C. Finally, 1% of trifluoroacetic acid was added to stop the reaction. The resulting peptides were purified using SDB-RP Stage tips (Sigma-Aldrich, Germany).

Prior to sample analysis, hMLKL isoform-specific peptides as well as loading controls shared by all isoforms were selected and corresponding stable isotope labeled spikes in peptides (SIL-peptides) were obtained in "SpikeTides" quality from JPT Peptide Technologies (Berlin, Germany). For the detection of the isoforms in HT-29 cells, a QExactive Exploris 480 mass spectrometer coupled to an Ultimate 3000 RSLC nano Ic system (ThermoScientific, Germany) was used for Sure Quant assays. Samples including 0.02 fmol/μl SIL-peptides were loaded onto a trap column (μ-Prepcolumn, Thermo Scientific, Germany) in 0.1% trifluoroacetic acid in water and backflush eluted onto an in-house packed C18-analytical column and chromatographically separated. MS1 survey scans were acquired from 400 m/z to 800 m/z at 120 000 resolutions. MS1 ions matching heavy peptide entries in the MS1 inclusion list were isolated in 1 m/z window and analyzed by fast MS2 survey scans that were acquired at 7 500 resolution with a maximum injection time of 10 milliseconds and an AGC target of 100%. High-quality MS2 target scans were triggered only when at least four MS2 ions matched the corresponding fragment ion reference list. Target scans were acquired at 60 000 resolutions, a maximum injection time of 116 milliseconds, and a 1000% AGC target. All scans were recorded in profile mode. Sure-quant data were analyzed as triggered acquisition experiments using the Skyline document that was prepared using runs of overexpressed MLKL isoforms.

Expression and purification of recombinant MLKL

Full-length mouse and human MLKL, their phosphomimetic versions (mMLKL2_S345D_S347D and hMLKL1_T357E_S358D and) and mMLKL2_I84A_F87A were expressed in Hi5 insect cells. Briefly, DNA encoding MLKL versions were cloned into a pFastBacderived vector as in-frame fusions with a TEV protease-cleavable N-terminal GST tag. Bacmids generated using the Bac-to-Bac system (Invitrogen, Germany) following the transformation of EMBacY *Escherichia coli* cells, were used to transfect Sf9 insect cells to generate the first baculovirus expansion (V0). Following two viral amplification steps (V1 and V2, 10% v/v), V2 was used to infect 0.8 L Hi5 cultures in flasks shaking at 300 rpm, 27°C for 72 h. Cell pellets were resuspended in buffer A (50 mM HEPES, 300 mM NaCl, 5% glycerol, 0.1% NP-40, 5 mM BME, pH 7.5) with protease inhibitors. Cells were lysed by sonication and cell debris was separated from soluble fraction via high-speed centrifugation for 1 h at 25000 g and 4°C . The supernatant was incubated with pre-equilibrated glutathione agarose beads (General Electric, Healthcare, Germany) at 4°C for 1 h with gentle agitation. Then, the beads were washed with 20 mL of buffer A to remove non-specific proteins. To achieve cleavage, glutathione agarose beads containing bound MLKL were incubated with 50 µM TEV at 4°C for 36 h. Elution was performed with buffer A and fractions were collected and loaded onto a Superdex 75 size-exclusion column (SEC) (General Electric, Healthcare, Germany) equilibrated with the same buffer. Proteins eluted from the SEC column were assessed for purity by Coomassie-stained SDS-PAGE. Proteins were then concentrated and flash-frozen for storage at -80°C .

Article



HDX mass spectrometry

Experiments were carried out on a fully automated HDX-2 system (supplied by Waters, CT, USA). The exchange reaction was started by diluting 4 μL protein sample with a concentration of 6 μM into 56 μL E-buffer for reference, or L-buffer for D2O labelling, and incubated for several time points (0, 30 and 1800 s). Subsequently, the exchange reaction was stopped by mixing 50 μL of sample with 50 μL precooled Q-buffer. Next, 95 μL of quenched sample was subjected to a temperature-controlled chromatography system equipped with a 50 μL sample loop (HDX nanoAqcuity UPLC, Waters, CT, USA). The protein was digested online by a Nepenthensin-2/Pepsin column (Affipro, Czech Republic). Eluting peptides were trapped and washed on a C18 pre-column (C18 1.7 μM VanGuard 2.1 x 5 mm pre-column; Waters, CT, USA) at 100 μL/min for 3 min and separated on a reversed-phase column (C18 1.7 μM Acquity UPLC 1 x 100 mm reverse phased column; Waters, CT, USA) with a linear gradient ranging from 5% ACN to 40% ACN plus 0.23% FA at 40 μL/min in 7 min, followed by a rapid rise to 95% ACN holding for 2 min. Then, columns were equilibrated with 95% H₂O plus 0.23% FA for 2 min. The reversed-phase chromatographic system was kept at approximately 0°C to reduce back-exchange. Peptides eluting from reversed phase column were measured with a Synapt G2-Si mass spectrometer (supplied by Waters, CT, USA) in HDMSE mode (50-2000 m/z). This mode contains ion mobility (IM) separation for 3D separation of the peptides (LC, IM, m/z). The mass spectrometer was fitted with an electrospray source equipped with additional independent LockSpray probe (GluFib lock mass solution, 785.8426 m/z) for alternating lock mass infusion. For data evaluation, non-deuterated peptides were identified using ProteinLynx Global Server 3.0.3. (PLGS, Waters, CT, USA) for each condition (control and binding). Only peptides with a high confidence score (over 6) identified in at least 5 out of 6 replicates (3 control and 3 binding replicates) were retained for further HDX evaluation. Peak picking of all corresponding peaks was performed with HDExaminer software package by Sierra Analytics. All mass spectra of every peptide, time points and replicates were manually analyzed and curated for correct peak identification. Next, all peptides which displayed statistically significance deuterium uptake differences, based on a Student's t-distribution with a 95% confidence interval (p \leq 0.05), in one out of two time points were used for further evaluation and visualization. Deuterium uptake difference maps created were plotted on our model of hMLKL1 using UCSF Chimera X.

MST experiments

Recombinant MLKL variants (hMLKL1, mMLKL2, and mMLKL2 I84A F87A) were labeled with Atto655 NHS ester dye using the standard protocol (ATTO-TEC GmbH-Siegen, Germany). MST experiments were performed on a Nanotemper Monolith NT.115 and analyzed using Originpro software (Microsoft, WA, USA). The inhibitors were incubated (in a concentration range of 7.6 nM -125 µM) with 100 nM Atto655-MLKL for 15 min in PBS with 0.05% Tween. Afterward, samples were loaded on glass capillaries and MST was performed using 80% excitation power and 40% MST power. Dissociation constants (Kd) were derived from the mass action equation using NanoTemper analysis software. Data were fitted in Originpro software following a 1:1 binding model.

ITC experiments

A stock solution of MBA-m1 was diluted in SEC buffer (50 mM HEPES, 300 mM NaCl, 5% glycerol, 5 mM BME, pH 7.5) to a concentration of 90 μM. Recombinant mMLKL2 was purified in the same SEC buffer and was further diluted to a concentration of 4 μM. 230 μL of mMLKL2 was loaded into the cell of a PEAQ-ITC instrument (Malvern Panalytical, Germany). 40 μL of MBA-m1 inhibitor was loaded automatically into the syringe. ITC measurements were carried out at 25°C using 750 rpm stirring speed and one 0.5 μL injection followed by twelve 3 μL injections. Two control experiments were carried out of MBA-m1 inhibitor against buffer, and these heats were subtracted from the MLKL experimental data according to the PEAQ analysis software (MicroCal, UK).

Vesicle preparation and permeabilization assay

Lipids were dissolved in chloroform and mixed in the proportion PC:PE:PA:PS:PI(4,5)P₂ (50:35:5:5:5) that mimics the composition of the inner plasma membrane. Films were prepared by evaporation of stock solutions using a stream of wet nitrogen and submitted to a vacuum for not less than 2 h. Then, lipids were resuspended in 80 mM calcein to achieve a 5 mg/mL final concentration and subjected to six cycles of freezing and thawing. Large unilamellar vesicles (LUV) were prepared using a two-syringe extruder (Avestin Inc., Canada), equipped with two stacked 100 nm polycarbonate filters (Nuclepore, UK). To remove untrapped fluorophore, the vesicles were filtered through mini-columns (General Electric, Healthcare, Germany) loaded with Sephadex G-50 (medium) pre-equilibrated (General Electric, Healthcare, Germany) with outside buffer (OB) (140 mM NaCl, 20mM HEPES, 1mM EDTA, pH 7.0).

LUV permeabilization was determined by measuring the fluorescence (λexc 490 nm and λem 520 nm) of released calcein. Black plastic 96-well microplates (Greiner Bio-one, Germany) were pre-treated with 2 mg/mL BSA (VWR, Germany), to reduce the unspecific binding of protein and vesicles to plastic. Each well was filled with different protein:inhibitor ratio, diluted in OB to achieve the following final concentration (50 µM MBA-h1, 20 µM MBA-m1, 50 nM hMLKL and phMLKL, 25 nM mMLKL2 and 6 nM pmMLKL2). Finally, the liposomes were added to complete a total volume of 200 μL. After mixing vesicles, protein, and inhibitor, the release of calcein produced an increase in fluorescence, F (because of the dequenching of the dye into the external medium), which was resolved in time. Spontaneous leakage of the dye was negligible under these conditions. Maximal release was always obtained by adding Triton X-100 (Sigma, Germany) at 1 mM. The percentage of calcein release was calculated by subtracting the values obtained due to spontaneous release and normalizing by the maximum intensity obtained in the presence of Triton X-100. Permeabilization rate (k) was calculated by fitting the curves to the equation: $y = A^*(1 - \exp(-k^*(x-xc)))$, using OriginPro 2018.



Analysis of Ripk1^{E-KO} samples

Skin sections were collected and prepared into a single-cell suspension according to previously described methods.⁵³ The singlecell suspensions of the skin were stained with a viability dye for 20 min at room temperature, followed by two washing steps with FACS buffer (5% FBS, 2 mM EDTA in PBS). A blocking with FC-receptor step was done for 10 min before CD16/CD32 monoclonal antibody incubation for 20 min at 4°C.Stained cells were then washed and fixed with BD CellFIX (BD Biosciences, Germany) for 30 min at 4°C before the samples were washed and resuspended in FACS buffer. CD4-AF488 and CD45-BV711 specific antibodies were used at 1:200 dilution for analysis, while Lys6G-PE was used at 1:800 dilution. Data was acquired using "LSR-Fortessa Analyzer" (BD Biosciences, Germany) and analyzed with FlowJo software (BD Biosciences, Germany).

Inflammatory cytokines (IL-1β, CCL3, and IL-6) were detected by enzyme-linked immunosorbent assay (ELISA). For this, protein extractions from frozen skin samples were prepared by dissociation with ceramic beads in extraction buffer (100 mM Tris, pH 7.4, 150 mM NaCl, 1 mM EGTA, 1 mM EDTA, 1% Triton X-100, and 0.5% sodium deoxycholate). Proteins concetration in the extracts was determines using a Protein Assay Dye Reagent (Bio-Rad, Germany). 50-80 μg protein from the extract were used for the ELISA, which was performed following the manufacturer's instructions (cat. nr: 88-7013-22, 88-56013-22, and 88-7064-22, Invitrogen, Germany).

Macroscopic assessment of skin lesions

Ripk1^{E-KO} and Tnfr1^{-/-};Hoil-1^{E-KO} mice were assessed macroscopically based on two main clinical criteria as described in.⁵ Each region of the body, comprising the head, neck, back, and flank, affected by lesions, was given a score of 1 and the sum of this provided information on how expanded the lesions were. The other criteria were the characteristics of the lesion: punctuated small crusts, coalescent crusts, and ulceration were assigned a score of 1 to 3, respectively. The sum of both criteria represented the total severity score of the lesions.

Immunohistochemistry of skin samples

For immunohistochemical (IHC) staining, skin biopsies were fixed in 4% paraformaldehyde (PFA) overnight at 4°C. Then tissues were embedded in paraffin and serially sectioned at a thickness of 5 µm. Sections were deparaffinized with serial washes in xylol and ethanol, and endogenous alkaline phosphatase was blocked using a blocking solution (BLOXALL®, Vector Laboratories, CA, USA). Antigen retrieval was performed by boiling in citrate buffer (pH 6.0) (Sigma-Aldrich, Germany) in a microwave, at 95°C for 6 min. Blocking was performed using 2.5% Normal Goat serum (Vector Laboratories, CA, USA) for 30 min at room temperature. Tissues were stained for CD45 (1:300) at 4°C overnight. Subsequently, slides were washed with PBS and incubated with ImmPRESS®-AP Goat Anti-Rat IgG for 30 min at room temperature. The signal was developed using Immpact Vector® Red substrate (Vector Laboratories, CA, USA) for 5 min. Slides were washed with dH₂O and counterstained with hematoxylin and eosin (Vector Laboratories, CA, USA), then washed, dried, and mounted using Neo-Mount (Sigma-Aldrich, Germany). Images were acquired using a Leica SCN400 slide scanner. For quantification, the epidermal thickness was measured on scans of full skin biopsies using a QuPath Software and measured every approximately 0.5 cm. The red signal of Immpact Vector® Red substrate (Vector Laboratories, CA, USA) was acquired using a fluorescent microscope (Evos FL Auto2, Life Technologies) in a red channel (Excitation: 365 nm -560 nm, Emission: Above 560 nm). Fluorescence intensity was calculated using ImageJ in five fields per section at 10x. After standard deparaffinisation and rehydration, the paraffin sections were retrieved Tris-EDTA based antigen retrieval buffer, pH 9 and then incubated with pMLKL-S345 (37333, Cell Signalling technology, MA, USA) antibody. All sections were counterstained with Haematoxylin (H-3401, Vector Laboratories, CA, USA) and then mounted using commercially available mounting media (H-5700, Vector Laboratories, CA, USA).

For the immunohistochemistry analysis of pMLKL, slides were digitalised via acquisition in a digital slide scanner (NanoZoomer S360MD Slide scanner system, Hamamatsu Photonics K.K.) with 20x magnification lens. Brightfield images used in th figures were acquired with Leica DM750 Binocular microscope and LAS X Life Science Microscope Software, Leica, objective 20x. The acquired digitalised images were analysed the open-source software QuPath.To quantify the positively stained cells, a pixel classifier was generated in order to exclude tissue areas that should not be accounted for during the quantification step and would otherwise interfere with the "positive cell detector" leading to false positive results. After setting the parameters and threshold, the "positive cell detector" was run and the quantification results were acquired.

Immunohistochemistry of abdominal aorta samples

Samples of the abdominal aorta were harvested, cleaned and embedded into Tissue-Tek O.C.T. Compound (Sakura Finetek™ 4583) and stored at -80°C for cryopreservation. The tissue was cut into 10 μm thick sections using a Leica CM3050 S Cryostat (Leica, Germany). Tissue sections were fixed with 4% paraformaldehyde (PFA) for 10 min and permeabilized using 0.1% Triton X-100 for 10 min at room temperature followed by blocking using 3% BSA for 1 h at room temperature. Tissue sections were incubated with primary antibody for anti-a smooth muscle Actin antibody (ab5694, Abcam) at 4°C overnight. Next day, the sections were washed three times in PBS followed by incubation with Alexa Fluor® anti-mouse CD68 Antibody (137020, BioLegend, CA, USA) or Alexa Fluor® 422 594 anti-mouse Ly-6G Antibody (127636, BioLegend, CA, USA) for 1 h at room temperature in the dark followed by washing and mounting. Cell nuclei were stained with DAPI. Images were acquired with a BZ-X800 microscope system (Keyence, IL, USA) and analyzed using ImageJ software.

Article



Modeling the 3D structures of the full-length mouse and human MLKL isoforms

Models were obtained using the MODELLER software package version 9.14.⁵¹ First, missing regions of the X-ray structure of the fulllength mMLKL2 (PDB: 4btf, residues 1-464) were modeled, since the absence of structural information in the crystal about these segments could mask important interactions of the C-terminus with other protein regions. Specifically, S79-K94 connecting helices 3 and 4 of the 4HB domain, the region Y118-Q128, located within the Br, and the K351-S358 and V456-V464 segments located in the psK domain were modeled. For this, the N-terminal domain of hMLKL1, solved by NMR (PDB: 2msv, residues 1-154) was superposed over the full-length mMLKL2 structure using the salign routine and the resulting alignment was used to model the 3D structure of mMLKL2. A similar methodology was used to model the full-length 3D structure of the mMLKL1 isoform. The 3D structure of the full-length hMLKL1 was modeled using as templates the X-ray structures of mMLKL2 (PDB: 4btf) as well as the N-terminal (PDB: 2msv) and psK (PDB: 4m67) domains of hMLKL1. First, the N-terminal and psK domains of the hMLKL1 were oriented properly through the structural alignment of both structures over the mMLKL2 structure with the salign routine and then the 3D structure of hMLKL1 was calculated with MODELLER based on the sequence-template alignment previously obtained. Specific positions in the psK domain of mMLKL1, mMLKL2, and hMLKL1 were mutated using RosettaScripts⁵⁴ to generate their phosphomimetic versions.

Molecular dynamics simulations

All MD simulations were carried out with the GROMACS software package version 5.1.455 using the AMBER99SB-ILDN force field and the TIP3P water model.⁵⁶ The simulation systems consist of one of the MLKL variants solvated in a dodecahedron box with ~37,000 water molecules. Electroneutrality was ensured by adding sufficient Na2+ or Cl- counterions to each solvation box. All the systems were relaxed through two consecutive energy minimization (EM), protocols. Then, each system was heated in the NVT ensemble and then equilibrated in the NPT ensemble at p=1 bar and T=310 K, keeping all the protein-heavy atoms restrained in both steps. Finally, the production NPT runs were conducted for 250 ns. The setup of EM and MD simulations was similar to that reported in a previous work.⁵⁷ A computational Ala scanning was performed with gmx_MMPBSA,⁵⁸ to rationally design mutations that affect the mMLKL2:MBA-m1 interaction without affecting the mMLKL2 activity.

Analysis of the MD simulations

All the structural analyses over the MD ensembles were carried out with the GROMACS 5.1.4 package. 55 For principal component analysis (PCA), the coordinates of MLKL variants recorded during the MD trajectory were first fitted to the starting structure to eliminate the overall translation and rotation, followed by the construction of the mass-weighted covariance matrix of atomic positional fluctuations of the backbone atoms of the equivalent residues among these systems. The covariance matrices were diagonalized to obtain the eigenvectors (PC) and eigenvalues (λ) that provide information about correlated motions throughout MLKL variants using the gmx covar and gmx anaeig tools. The first vector (PC1) describes the expansion of the psK domain together with the compaction of the whole structure, as well as the stabilization of the brace helices into a unique conformation. It captured 24.8% of the structural variation of the mMLKL along the MD simulation. The second vector (PC2) described the motions within the 4HB, the activation loop, and the loops connecting the 4HB, Br, and psK domains. The models were built using the first 90 ns of the MD simulations, while the remaining 160 ns were used for cross-validation. Root-Mean-Square Deviation (RMSD) values and their distributions were calculated with the gmx rms and gmx analyze programs. 55 The distance between specific pair of residues within MLKL structure was calculated with gmx distance. The frequency of contact of MLKL residues with each inhibitor was computed with the gmx select using as cutoff 0.4 nm.

Structure-based virtual screening

To identify putative MLKL blockers the Tres Cantos Antimalarial Set (TCAMS) available at the Chembl-NTD database (http://www. ebi.ac.uk/chemblntd) was screened with the Autodock Vina software⁵⁹ using the Hc/groove of hMLKL1 or mMLKL2 as target. For each compound, ten poses were generated and ranked with the scoring function of the Autodock Vina software. The side chains of residues Tyr23, Asn81, Arg82, Cys86, and Phe148 were treated as flexible in the virtual screening simulations of the hMLKL1. We selected the best-ranked commercially available compounds for human and mouse MLKL based on the scoring function of this initial analysis and tested them in necroptosis inhibition assays. We excluded Pan Assay Interference Compounds using the PAINS-Remover web server (http://cbligand.org/PAINS).60

QUANTIFICATION AND STATISTICAL ANALYSIS

Blots and images are representative of at least three independent experiments. All measurements were performed at least three times, and results are presented as mean ± SD. Box-plot elements are defined as: center line are medians, squares are means, box limits are upper and lower quartiles, whiskers ranges correspond to the 1x SD and individual points correspond to values obtained from independent replicas. All statistical tests were carried out using GraphPad Prism 10 software. p values from significantly different conditions are shown. Samples were compared to the one indicated with the minor tick. Significance was calculated using t-Test paired two samples for the means, otherwise specified in the figure legend.